IEEE Access
Multidisciplinary | Rapid Review | Open Access Journal

Received May 29, 2021, accepted June 13, 2021, date of publication June 21, 2021, date of current version July 15, 2021.

Digital Object Identifier 10.1109/ACCESS.2021.3090825

Recent Automatic Segmentation Algorithms of MRI Prostate Regions: A Review

ZIA KHAN[1], NORASHIKIN YAHYA[1], (Member, IEEE), KHALED ALSAIH[2], MOHAMMED ISAM AL-HIYALI[1], AND FABRICE MERIAUDEAU[3], (Member, IEEE)

[1]Centre for Intelligent Signal and Imaging Research, Electrical and Electronic Engineering Department, Universiti Teknologi PETRONAS, Seri Iskandar 32610, Malaysia
[2]CNRS, IOGS, Université de Lyon, UJM-Saint-Etienne, Laboratoire Hubert Curien, UMR5516, 42023 Saint-Etienne, France
[3]ImViA/IFTIM, Universite Bourgogne Franche-Comté, 21000 Dijon, France

Corresponding author: Norashikin Yahya (norashikin_yahya@utp.edu.my)

This work was supported in part by the Yayasan Universiti Teknologi Petronas under Grant YUTP-FRG 015LC0-292, and in part by the Imagerie et Vision Artificielle (ImViA) / Imagerie Fonctionnelle et moléculaire et Traitement des Images Médicales (IFTIM) Research Grant.

ABSTRACT World-wide incidence rate of prostate cancer has progressively increased with time especially with the increased proportion of elderly population. Early detection of prostate cancer when it is confined to the prostate gland has the best chance of successful treatment and increase in surviving rate. Prostate cancer occurrence rate varies over the three prostate regions, peripheral zone (PZ), transitional zone (TZ), and central zone (CZ) and this characteristic is one of the important considerations is development of segmentation algorithm. In fact, the occurrence rate of cancer PZ, TZ and CZ regions is respectively. at 70-80%, 10-20%, 5% or less. In general application of medical imaging, segmentation tasks can be time consuming for the expert to delineate the region of interest, especially when involving large numbers of images. In addition, the manual segmentation is subjective depending on the expert's experience. Hence, the need to develop automatic segmentation algorithms has rapidly increased along with the increased need of diagnostic tools for assisting medical practitioners, especially in the absence of radiologists. The prostate gland segmentation is challenging due to its shape variability in each zone from patient to patient and different tumor levels in each zone. This survey reviewed 22 machine learning and 88 deep learning-based segmentation of prostate MRI papers, including all MRI modalities. The review coverage includes the initial screening and imaging techniques, image pre-processing, segmentation techniques based on machine learning and deep learning techniques. Particular attention is given to different loss functions used for training segmentation based on deep learning techniques. Besides, a summary of publicly available prostate MRI image datasets is also provided. Finally, the future challenges and limitations of current deep learning-based approaches and suggestions of potential future research are also discussed.

INDEX TERMS MRI, prostate cancer, deep learning, automatic algorithms, prostate gland.

I. INTRODUCTION

Prostate cancer is a significant global public health issue and has ranked as the second world's prevalent cancers in male after lung cancer. Diagnosis of prostate cancer has become a challenging task with a progression rate of 1 in 6 men affected throughout their lives, and 1 in 36 died from the disease, being the second most common cause of death among men [1], [2]. According to the study in [3], prostate cancer ratio is the highest in the United States (USA) at 21% whereas it ranges from 1 to 9 in 100,00 men in Northern Europe, North America, New Zealand, and Australia. In 2019, among the various types of cancer, including breast cancer, lung cancer, colon, and rectum cancer, prostate cancer has recorded 174,650 new prostate cancer cases, and 31,620 cancer deaths in the U.S. [4]. The survival rate of individuals affected with prostate cancer is relatively high. However, human aging factors would exacerbate the disease and spread cancer to other organs if left untreated.

Most prostate tumors start out as benign tumors which does not have cancerous cell and grow gradually in size, whereas malignant tumors have cancerous cell and grow at a

The associate editor coordinating the review of this manuscript and approving it for publication was Zhipeng Cai.

faster rate [5]. Around 85% of diagnosed prostate cancers are restricted to the prostate gland PZ [6]. The PZ covers 70-80% of total prostate size, in which if there is a malignant tumour, it is usually less aggressive than the ones in the CG [7].

In general, the prostate cancer severity level is divided into 4 stages. In stage I, the cancer cells are localized in the prostate gland and develop at a gradual rate [8]. Cancer cells in stage II develop faster compared to stage I. In stage III, cancer cells have spread to tissues surrounding the prostate gland, while in stage IV, the cancer cells have metastasized to other tissues such as lymph nodes and the rectum.

Prostate cancer primary signs are enlisted in [9]–[11], but the leading cause of prostate cancer is still unclear. A preliminary list of risk factors is drawn up from ongoing work to classify prostate cancer [12]. The etiology is related to the following factors: (i) history of the family, (ii) genetic factors, (iii) ethnicity, (iv) diet and (v) obesity [13], [14]. It is recommended that people conduct the daily physical exercise, eating green vegetables, fish, vitamin E and mineral supplements to avoid prostate cancer [15]. A prostate cancer diagnosis cannot be based solely on risk factors, so allowing screening makes it possible to detect and treat early. Patients at the early stage of prostate cancer are most often asymptomatic. However, a common symptom is bladder outflow obstruction, indicating blockage of the urinary flow due to the tumour pressing against the urethra.

The article is outlined as follows. In Section II, reviewed papers related to prostate anatomy, prostatic carcinoma, are described. Next, Section III prostate screening and imaging techniques, Section IV image pre-processing techniques and Section V provides review of prostate MRI segmentation methods, Section VI prostate segmentation techniques related papers. Section VII the impact of multiparametric MRI and evaluation techniques. Section VIII Overview of clinical application of deep learning for prostate MRI segmentation and cancer detection. Lastly, Section X summarizes the challenges, future perspectives and concludes the overall review work.

To identify related contributions, different digital databases such as Scopus, PubMed, scienceDirect, IEEExplore are utilized to collect important literature. The query for papers containing is ''convolutional,'' ''deep learning,'' ''prostate,'' and ''image segmentation'' in title or abstract. Additionally, conference proceedings for MICCAI PROMISE1-12, I2CVB, NCI-ISBI, PROSTATEx, and PROSTATEx2 are searched based on each paper's title. The most recent paper reviewed in this article is the one published on December 2020 [16]. There are several steps applied to filter and select important articles in topic. First step is removing duplicated publications among digital databases. Next, the titles and abstracts of the publications were checked to examine the relevancy of the selected articles. Then, full-text reading to find out whether they are appropriate to be involved in the final set. finally, only 110 articles met all criteria and were considered fit for inclusion in this review.

II. BACKGROUND

This section provides an overview of prostate anatomy, prostatic carcinoma, prostate screening, imaging techniques, and MRI modalities.

A. PROSTATE ANATOMY

The prostate is the gland in the male reproductive organ, and its primary role is to generate fluid that protects and enriches sperm. In general, prostate gland is described as being like a walnut in shape and size, located below the bladder and in front of the rectum.

The prostate approximate height and depth are 3 cm and 2.5 cm, respectively. Besides, the prostate weight is estimated to be in the range of 7-16 grams in adults [17]. As human starts to grow, the initial increase in prostate size occurs during puberty. The prostate size increases after the age of 60 [18], which causes benign prostatic hyperplasia (BPH).

The internal structure of the prostate is explained by several researchers in [19]–[21]. In the article by McNeal [21], 3D zonal classification of the prostate gland is performed, showing that the prostate is a glandular organ having four heterogeneous regions as listed below:

1) Anterior fibromuscular stoma having no glandular tissue.
2) TZ consists of 5% of glandular tissue.
3) CZ contain 20% of the glandular tissue.
4) PZ contains 70% to 80 % of glandular tissue.

In prostate cancer imaging, the three different zones are observed, subdivided into the TZ, PZ, and CZ. The CZ and TZ look similar in medical imaging and collectively named as a central gland.

B. PROSTATIC CARCINOMA

Countries having a high socio-demographic index have a high ratio of diagnosing prostatic Carcinoma or prostate cancer. The prostate cancer or carcinoma is a glandular cancer, and it is available in the different zones of the prostate at different ratio [22]. McNeal *et al.* [7] experimented 104 ex-vivo prostate gland, after radical prostatectomy, for zonal distribution of prostate cancer where tumors are outlined and their volume is mapped and determined using the Gleason score [23]. Also, the relative location of the gland with respect to the transition zone is determined in the study. It is established that prostate cancer is more likely to come in a specific region of the prostate. The probability of cancer cells occuring in three different zones; CZ, PZ, and TZ are 10%, 70%, and 20%, respectively. Since cancer cells are more likely to develop in the PZ, segmentation of the PZ is critical in diagnosing prostate cancer.

III. PROSTATE CANCER SCREENING AND MRI IMAGING TECHNIQUES

Initial examination and screening of prostate cancer abnormalities in the prostate gland are performed by prostate-specific antigen (PSA) and digital rectal examination (DRE).

PSA concentrations are not conclusive evidence for the existence or absence of prostate cancer. Elevated PSA does not indicate cancer; in noncancerous circumstances, such as benign prostatic hyperplasia, PSA is also present. Acute and chronic prostatitis and physical trauma and inflammation affect PSA levels. It is challenging to determine PSA testing accuracy since men with typical PSA values will not undergo biopsy unless their DRE is abnormal. PSA rates between 4–10 ng/ml do not give physicians the clarity to perform biopsy [24], [25]. Consecutive biopsy procedures are invasive and can create several risks for the patient. Therefore, health care institutions thrive on eliminating the risks related to biopsy. The prostate health index (PHI) test [26], [27] is performed to minimize the possibility of negative biopsy. The prostate health index results are based on a score that provides information on the probability of having a prostate cancer and confidence in biopsy decisions [28]. However, with the availability of MRI, accurate localization of the cancerous tissues inside the prostate can be performed, thereby limiting the numbers of unnecessary biopsies [29]. Besides, accurate localization of cancerous tissues within the prostate gland during surgery or radiotherapy treatment help avoid damaging the surrounding tissues [22].

Computed tomography (CT) and transrectal ultrasound (TRUS) are often used to assess prostate cancer regions. CT scan is mainly used in case that prostate cancer has reappeared after treatment, and help to determine if the cancerous regions are growing into other organs. On the other hand, TRUS is used to guide a needle during a biopsy and estimate the prostate size and shape. Both CT and TRUS have lower resolution than MRI; hence, imaging soft-tissue contrast is not well-defined resulting in critical information lost during the early assessment of prostate cancer [30]. Magnetic resonance imaging is a promising imaging technique. The biopsies executed using MRI are more accurate and less harmful than the biopsy using TRUS [31]. MRI is very popular in detecting and staging prostate cancer because it provides better soft-tissue contrast, better resolution and it is a radiation-free modality. The main disadvantages of MRI are the high cost, and long acquisition time when imaging is required. Further details on different MRI sequences are elaborated in Subsections III-A,III-B III-C.

A. T1 WEIGHTED MAGNETIC RESONANCE IMAGING (T1W MRI)

T1W is an imaging protocol that depends on the longitudinal relaxation of tissue's net magnetization vector (NVM). T1W MRI is unable to clearly show the prostate anatomic structure, so it is mainly used for the detection of post-biopsy bleeding. A sample of T1W prostate MRI is shown in Figure 1.

B. T2 WEIGHTED MAGNETIC RESONANCE IMAGING (T2W MRI)

T2W MRI is an imaging protocol that highlights differences in the T2 relaxation time of tissues. T2W MRI is employed on a priority-based MR imaging tool for non-invasive prostate cancer diagnosis, localization, and staging due to the better resolution and contrast provided [32]. T2W MRI is usually performed in three planes; axial, coronal, and sagittal where cancerous cells appear different in terms of intensity and homogeneity [33]–[35]. The PZ is homogeneous and hyperintense in normal tissue. In contrast, in malignant tissue, the PZ has low intensity, and both PZ and CG are homogeneous in malignant tissue compared to healthy tissue [35], [36]. T2W MRI leads to better recognition of the three prostate zones; PZ, TZ, and CG [37] are shown in Figure 2.

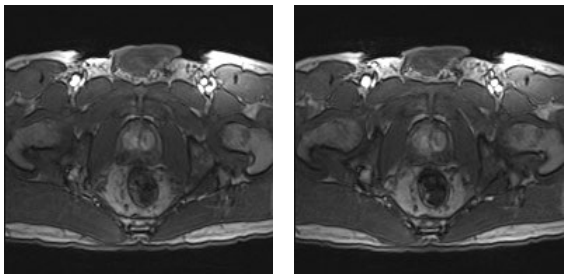

FIGURE 1. 2D prostate T1W MRI.

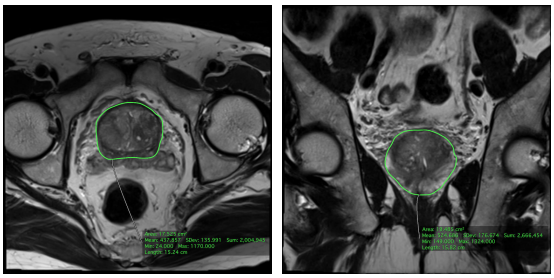

(a) (b)

FIGURE 2. 2D prostate T2W MRI (a) axial view, (b) coronal view. The prostate boundary is marked by the green line.

C. DIFFUSION-WEIGHTED MRI (DW MRI)

Diffusion-weighted MRI is the advanced MRI technique to study and diagnose prostate cancer [38]. DW-MRI discerns water molecules movement by exploiting the variation in the movement of water molecules in various soft tissues [39]. The growth of prostate cancer demolishes the regular gland structure and increases cellular density [40], [41]. Higher cell density has an inverse relation with the diffusion of water molecules [41], [42]; therefore, water movement are restricted in prostate cancer regions as compared to healthy regions [40], [41]. Hence, water molecules diffusion ratio helps better differentiate between healthy and non-healthy tissue, as shown in Figure 3. The magnetic gradient is utilized to detect the problem in nuclei spatial location in DW MRI; by introducing a magnetic gradient, which dephase the water molecules movement in nuclei [43]. The dephase of water movement varies among different gradient intensity in a different location. The second magnetic gradient is applied to cancel the spin dephasing. The restricted water molecules

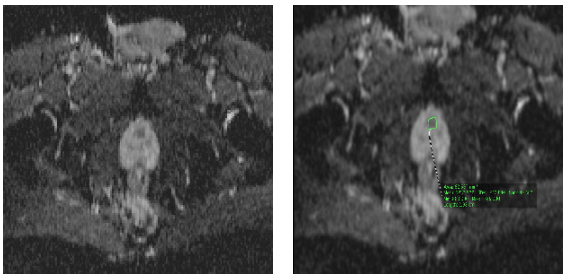

(a) (b)

FIGURE 3. Diffused Weighted T2W MRI in (a) and its ADC map in (b).

will meet the same gradient intensity while the moving water molecules will face different gradient intensity. The second magnetic causes the moving water molecule to dephase while immobile water molecules in phase. The higher the random motion will cause more loss in signal than lower random motion [44]. The signal loss is formulated

$$S_{(b)} = \exp(-b \times ADC), \tag{1}$$

Here, the b variable represents the attenuation coefficient and ADC shows apparent diffusion coefficient. When the value of the attenuation coefficient is zero, then DW MRI is similar to T2W MRI. In equation 1, different ADC maps can be generated by varying the b value.

IV. IMAGE PRE-PROCESSING TECHNIQUES

A. IMAGE DENOISING

In MRI images, multiplicative or additive noises can occur. Thermal noise is the primary source of noise in MRI images [45]. Thermal noise can be modelled as an additive, white, and stationary Gaussian random process with zero mean. The discrete inverse Fourier (DF) transformation reconstructs the MRI. Since linearity and orthogonal concepts, the MRI image has imaginary and real parts influenced by Gaussian noise. The magnitude component of the MRI is affected by the Rician noise. The Rician distribution is similar to a Rayleigh distribution [46] when SNR is low, while at high SNR, it looks like a Gaussian distribution [47]. Various filters have been used to decrease the noise, for instance, Ozer *et al.* [48] used the classical median filter; however, it removes the information of minute structures. Bilateral filter [49] performs better noise removal, but faces problems in low-frequency region. More sophisticated methods have been suggested to solve this issue. Ampeliotis *et al.* [50], [51] use wavelet shrinkage [52]. More recently, Non-local mean (NLM) [53] has shown better performances, but suffers from a high computational time. BM3D filter [54] performs a better trade-off compared to NLM or Bilateral Filter other techniques as it requires less computational time and maintain good image quality.

B. IMAGE NORMALIZATION

Intensity normalization is applied to reduce variation in the intensity distribution of MRI images, in which inter-patient variability occurred [55]. The application of intensity normalization also improves the comparability of images across different subjects, resulting in better segmentation results. The variation of intensity can be corrected by scaling the intensity values using the min-max technique and z-score normalization [55], [56]. Min-max approach [56] normalizes the data by subtracting the minimum value from the image intensity, and then divide it by subtraction of maximum and minimum values. The minimum and maximum values are transformed 0 and 1, respectively, while the remaining value is converted into a decimal value between 0 and 1. Equation describing normalized intensity, $I_n(i)$ is given by

$$I_n(i) = \frac{I_r(i) - min(x)}{max(x) - min(x)}, \tag{2}$$

where $I_r(i)$ shows the intensity before normalization, $min(x)$ and $max(x)$ shows the maximum and minimum values of the intensity. Z-score normalization [55] preformed the normalization of images by subtracting the mean from the signal intensity and then divided by the standard deviation of the signal intensity. Equation of z-score normalization intensity, $I_n(i)$ is given by

$$I_s(x) = \frac{I_r(x) - \mu}{\sigma}, \tag{3}$$

where $I_r(i)$ shows the intensity before normalization, similarly, the μ and σ are the mean and standard deviation of the signal intensity, respectively.

In prostate MRI scan, the size of prostate gland is comparatively small to the background region, and this factor would result in poor segmentation of the prostate [57]. Thus, center-cropping technique is employed to reduce the number of background pixels, eliminating the redundant pixels and as a result reducing computation time.

C. DATA AUGMENTATION

In medical imaging datasets, large number of training labels are not available for several reasons. The image delineation in the data set requires an expert (radiologist), which is time-consuming and expensive. When deep neural networks are trained from limited training data, the over-fitting problem transpires [58]. Data augmentation is a practical approach to reduce over-fitting and increase the amount of training data. The training dataset is augmented by generating new images using various operations, such as rotation, translation, scaling, and flipping. Then original and augmented images are used for training the deep convolutional neural network (DCNN).

V. MRI SEGMENTATION METHODS

In this review, the articles based on machine learning (ML) and deep learning (DL) are elaborated. General methodology for prostate segmentation algorithm development using machine learning and deep learning is illustrated in Figure 4. In Figure 5 groups major techniques of prostate segmentation based on ML and DL approaches.

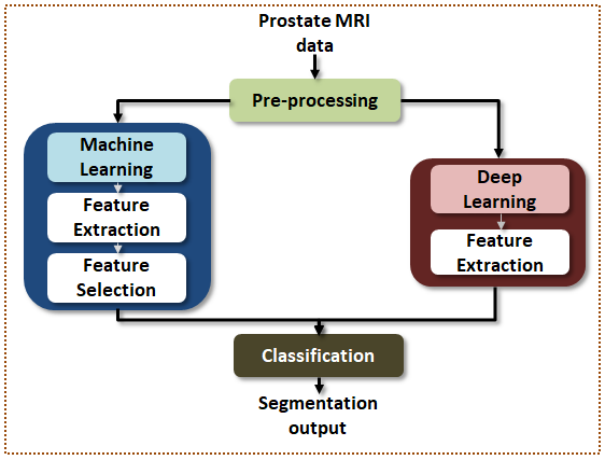

FIGURE 4. General methodology of machine learning and deep learning approaches in prostate segmentation.

A. MACHINE LEARNING-BASED SEGMENTATION

1) ATLAS-BASED SEGMENTATION

Atlas is constructed by a collection of manual segmentation anatomical structures registered in a specific frame of coordinates. The atlas then serves as a reference for a new patient image segmentation. For this reason, the segmentation problem is treated as a registration problem in atlas-based segmentation. Thus, mapping a pre-segmented atlas image to the target image is implemented to perform the atlas segmentation.

2) DEFORMABLE MODEL-BASED SEGMENTATION

Geometry, physics, and mathematical optimization theories influenced the deformable model segmentation. Geometry puts constraints on the form of the object. Physical methods direct the evolution of the structure in space, and the principle of optimization guides the object to match the available data [59]. The internal and external energy has direct impacts on deformable models. External energies help locate the boundary with the deformable model, while internal energies preserve the smoothness of the contour during deformation.

B. DEEP LEARNING-BASED SEGMENTATION

Recent works in deep learning for semantic segmentation has shown remarkable results. This section provides overviews of 4 groups of DL-based semantic segmentation that are applied in segmenting prostate regions and detecting prostate cancer. The approaches are divided into four groups: feature encoder, upsampling, resolution increment of features, and regional proposal-based segmentation techniques.

1) FEATURE ENCODER-BASED TECHNIQUES

Feature encoder-based techniques are the pioneer of deep learning models that are employed to classify distinct objects. The basic concept of feature encoder techniques is the extraction of features from the input data. Stack of convolutional layers, activation function (ReLU), and pooling layers are applied for feature extraction. The feature encoder based techniques utilize the trained models over different datasets and retrain the last layer with the new input. The AlexNet [60], VGG [61], ResNet [62], and Xception [63] pre-trained models are the most prevalent methods for feature extraction. The founder of the deep CNN network (AlexNet) that won the ImageNet large scale visual recognition challenge (ILSVRC) with as the top-5 test accuracy of 84.6%, Krizhevsky *et al.* [60] introduced the architecture, consisting of five convolution layers, max-pooling layers, rectified linear units (ReLUs) as non-linear, three fully-connected layers, and dropout. Later in 2014, the University of Oxford Visual Geometry group launched the VGG network [61] and becomes the runner up for ImageNet ILSVRC. Instead of using larger receptive fields with few convolution layers, such as LeNet [64] and AlexNet [60], VGGNet applies several 3×3 convolution with limited receptive fields. However, due to prediction at each pixel level, applying CNN architectures for segmentation requires a dense layer with large number of parameters making it computationally expensive.

He *et al.* introduced ResNet [62], which uses residual blocks in their architecture as the main building block. ResNet is the neural network that consists of deep neural network with large numbers of layers most commonly used for semantic segmentation. It is hard to train a deep neural network with a large number of layers. The network efficiency starts degrading due to the vanishing gradient problem with an increase in the network depth. By adding skip connections, He *et al.* [62] effectively solved the problem of the vanishing gradient. In addition, novel residual blocks are implemented in which the gradients can easily flow through the shortcut connection during the passing of back propagation without any issue. Furthermore, Google has updated Inception model [57] with a depthwise-separable convolution layer and built an extreme version called Xception network [63]. The depthwise-separable convolution performs channel-wise convolution (depthwise convolution) and 1×1 convolution (pointwise convolution), producing a lighter and less computational network.

2) UPSAMPLING-BASED TECHNIQUES

The CNN models utilize a convolution block to generate feature maps on successive convolutional layers but this will result in loss of spatial or location information. To address this issue, first, the spatial information lost during the operation of downsampling can be recovered by upsampling and deconvolution. Secondly, the development of reconstruction approaches for combination low- and high-level features to improve the spatial accuracy and optimization techniques. Noh *et al.* [65] made use of the principle of upsampling to build a deconvolution network. The convolution network reduces the size of feature maps in every convolution layer. In contrast, the upsampling network enlarges the feature maps by applying unpooling and deconvolution operations on every input feature map from the convolution block.

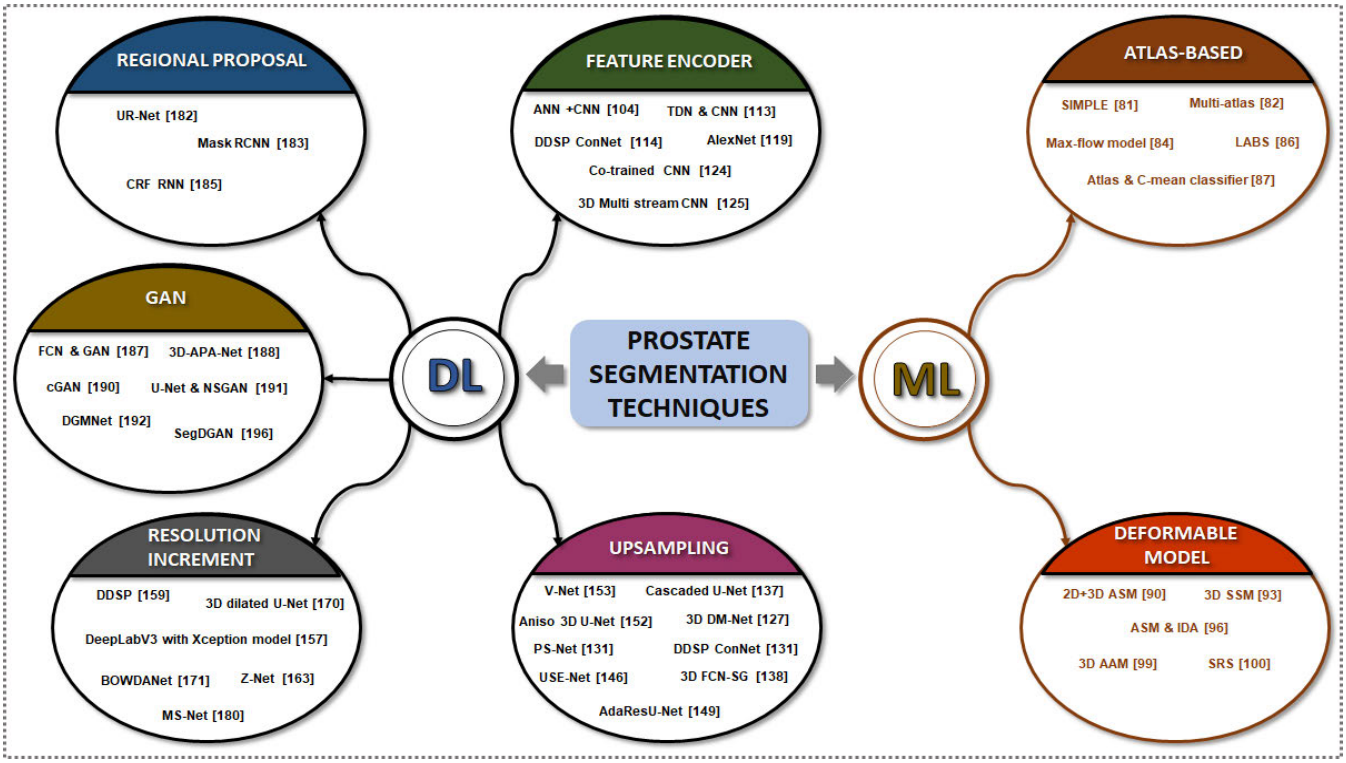

FIGURE 5. Categories of deep learning and machine learning techniques for prostate segmentation.

With the fully convolutional network (FCN) implementation, Long *et al.* [66] enabled breakthroughs in deep learning-based semantic segmentation. FCN uses CNN architecture and modifies the classification network [57], [60], [61] into a fully convolutional network, generating a projected output for arbitrary size. U-Net [67] is another prominent fully convolutional neural network, which has been developed for medical image segmentation. The encoder part consists of successive convolution followed by an activation function (ReLU), while the decoder part consists of an upsampling layer, which is connected with the encoder by skip connection. Badrinarayanan *et al.* [68] developed an encoder-decoder, fully convolutional neural network called SegNet. The encoder network is identical, like VGG [61], having no fully connected layers followed by a decoder network from [69] for pixel-wise classification. SegNet performed very well in scene and natural image segmentation tasks.

3) RESOLUTION INCREMENT OF FEATURE-BASED TECHNIQUES

Resolution increment of feature enhanced the resolution of feature maps by gathering sufficient information from the input images with larger receptive fields. The receptive field can be larger by using a special type of convolution called atrous convolution. The atrous convolution [70] recovers the spatial resolution and generates high-resolution feature maps for dense prediction. The atrous convolution adds a specific characteristic to the convolution layer, called "dilation rate," and can extend the receptive field without losing resolution. Chen *et al.* [70] developed DeepLab, a deep convolution neural network. Instead of using deconvolution, atrous convolution is applied. Later, Chen *et al.* [71] re-examined atrous convolution and developed a new model called DeepLabV3. The new network was developed in which atrous convolution is performed parallel by adopting multiple atrous rates to collect multi-scale information. The last block in ResNet [62] was arranged in a cascaded manner. Inspired by Alvarez *et al.* [72], Chen *et al.* [73] has extended the DeepLabV3 version and launched the new DeepLabV3+ network. In particular, the work employed a decoder module with encoder features upsampled by a factor of 4 instead of 16, as in [71]. The corresponding low-level features from the network backbone with the same spatial resolution are then concatenated. The Xception model [63] has been adopted and applied to both atrous spatial pyramid pooling (ASPP) and decoder modules with a depth-wise separable convolution. Compared to regular convolution with larger filters, atrous convolution effectively enlarges the field of view of filters without increasing the computational time. In complex prediction tasks, dilated convolution is a simple but robust alternative to deconvolution.

4) REGIONAL PROPOSAL-BASED TECHNIQUES

Regional proposed networks (RPNs) have been developed to detect objects in images using selective search method.

The RPN generates a proposal for objects in the images using scales and aspect ratios. The generated proposals are then utilized to classify the objects. Girshick *et al.* [74] implemented the first region-based convolutional neural network (R-CNN) for the detection of objects. The R-CNN applied a selective search method [75] that extracts 2000 different regions from an image having the highest probability of containing an object. CNN [64] extracts the features of each region, which is then fused with created regions. At last, the support vector machine (SVM) classifies the features into a set of classes. Girshick *et al.* [76] modified the architecture of R-CNN [74] with RoI pool (Region of Interest Pooling) and named the network Fast RCNN. The RoI Pool (Region of Interest Pooling) has improved and increased the training and testing speed of the network. Furthermore, the microsoft team proposed a Faster RCNN [77] architecture. They presented a region proposal network (RPN), which generates region proposals with multiple scales and aspect ratios. The feature maps of RPN are forwarded to Fast RCNN for object detection. The RPN and Fast RCNN together increase the accuracy and decrease the computational cost. He *et al.* [78] performed pixel-level image segmentation by extending Faster R-CNN to a Mask regional convolutional neural network (Mask-RCNN). The FCN is fitted on each ROI to extract features for predicting an object mask in a pixel-to-pixel manner, in parallel with the existing branch for bounding box recognition. Moreover, in mask RCNN, the RoI pooling layer is replaced with region of interest alignment (RoIAlign), that preserves exact spatial locations.

VI. PROSTATE MRI SEGMENTATION TECHNIQUES - RELATED PAPERS

Radiologist workloads have been increasing over the years in line with an increasing number of cancer patients. One of the time-consuming tasks is zonal segmentation of prostate gland for assessing the severity of tumor or cancer staging. Besides, reviewing MRI scans for cancer staging can be time consuming and error prone. The goal of automatic segmentation techniques is to help reduce doctors' workloads and improve patient outcomes. In this section, we have highlighted some crucial works on prostate segmentation based on machine learning and deep learning techniques.

Computer-based innovations have played a significant role in the area of medical applications. The automatic and semi-automatic methods help the physicians in management and analysis of clinical data. Visualisation technologies demonstrate great value in simulation and real-time application of clinical procedures. Before the breakthrough of deep learning, automatic and semi-automatic machine learning-based techniques were implemented for segmentation of prostate MRI images. Many researchers have applied machine learning-based techniques, most common ones are atlas-based and deformable model-based for segmentation of prostate gland MRI images.

The arrangement of this section is according to the categories of DL and ML segmentation techniques as shown in Figure 5. The first two sections cover segmentation of prostate grouped into atlas-based and model-based techniques. The subsequent three sections cover segmentation of prostate based on deep learning techniques, arranged in 5 groups of DL-based segmentation, feature encoder, upsampling, resolution increment, regional proposal and GAN. Also, a section for multi-parametric MRI on segmentation and prostate cancer detection is also included.

A. ATLAS-BASED PROSTATE MRI SEGMENTATION - RELATED PAPERS

A summary of atlas-based prostate segmentation methods is tabulated in Table 1. The abbreviation of private (Pv) dataset are the ones originating from independent research groups that had acquired sufficient patient data and providing the ground truth for training and testing of tha algorithm. Most of the time, these data are not publicly available. The performance segmentation are listed using DSC values whereas for papers, where the work also involved classification of prostate cancer, accuracy (ACC) of the detection is reported.

In the early work of atlas-based prostate segmentation, from 2008 to 2010, proposed methods [79]–[82] was focussing on segmenting the WG of the prostate rather than segmenting the different parts of the prostate. Only at the beginning of 2012, with the increasing need for zonal segmentation, proposed atlas-based segmentation methods were developed for separating the different parts of the prostate [83]–[88].

Klein *et al.* [79] performed segmentation of the prostate gland using multi-atlas segmentation where the localized mutual information similarity measure is utilized to match manually segmented atlas with the images. Martin *et al.* [80] has introduced the probabilistic-based automatic segmentation of the prostate gland 3D MRI images. Probabilistic segmentation is achieved by registering a new image to a probabilistic atlas and applying a statistical shape model and feature model to refine prostate gland segmentation. Langerak *et al.* [81] presented an atlas-based approach using geometric transformation to register image samples with the related mask to the target image. The iterative method for performance level estimation (SIMPLE) is utilized to generate required labels from the deformed labels to perform prostate gland segmentation. Dowling *et al.* [82] developed the multi-atlas label fusion approach to localize the prostate region in MRI images. The fused multi-atlas are mapped to each MRI scan using rigid, affine and non-rigid registration.

Litjens *et al.* [83], implemented the method of Klein *et al.* [79] using multiparametric MRI and evaluated the segmentation method by majority voting and simultaneous truth and performance level estimation (STAPLE) [89]. Qiu *et al.* [84] performed segmentation of prostate glands by employing a global optimization technique. Giannini *et al.* [85] developed a two-stage process: probability maps are generated using prostate volume, and then using the generated maps, segmentation is performed to locate the suspected area of prostate gland. Zhang *et al.* [86]

TABLE 1. Summary of the atlas-based prostate segmentation, cancer detection techniques and their performance.

Paper No.	Year	Dataset		No of Images	Pre-processing Technique	Technique	Performance				DSC or accuracy
		Pv	Pro 12				WG	PZ	CG	ACC	
[79]	2008	✓		50	•Registration	•Atlas matching	✓				0.87
[80]	2010	✓		36	•Resampling	•Atlas-based approach	✓				0.86±0.02
[81]	2010	✓		100	•Registration	•STAPLE •SIMPLE				✓	0.90
[82]	2011	✓		50	•Bias field correction •Histogram equalization	•Multi-atlas •Gradient anisotropic diffusion	✓				0.86±0.02
[83]	2011	✓		48	-	•Multi atlas-based segmentation		✓	✓		0.75±0.07, 0.89±0.03
[84]	2014	✓		18	-	•Continuous max-flow model	✓	✓	✓		0.89±0.03, 0.70±0.06, 0.830±0.02
[85]	2015	✓		88	•Normalization •Registration	•Probability maps	✓				0.91
[86]	2016	✓		100	•Interpolation •Registration	•LABS	✓		✓		0.85±0.03, 0.77±0.06
[87]	2016		✓	50	•Registration	•Atlas-based approach •C-mean classifier	✓	✓	✓		0.817±0.05,0.70±12.06,0.62±0.07
[88]	2016	✓		13	•Normalization •Noise reduction	Multi-atlas-based approach	✓				0.895±0.02

Dataset: Pv-Private, Pro-12-PROMISE12.

TABLE 2. Summary of the deformable model-based prostate whole gland (WG) segmentation techniques and their DSC values.

Paper No.	Year	Dataset			No of Images	Pre-processing Technique	Technique	Performance	
		Pv	Pro 12	NCI ISBI				WG	DSC
[90]	2005	✓			26	•Normalization	•2D ASM •3D ASM	✓	0.87
[91]	2009	✓			26	•Normalization	•Statistical shape model	✓	0.93±0.3
[93]	2009	✓			20	•Normalization	•3D SSM	✓	0.83±0.09
[92]	2010	✓		✓	60	•Registration	•Deformable model •Global registration	✓	0.84±0.03
[95]	2012	✓			50	•Cropping •Bias field correction	•Deformable model	✓	0.84±0.012
[96]	2012	✓			108	•Normalization •Interpolation •Scaling	•ASM •IDA	✓	0.88±0.7
[97]	2012	✓			522, 29	•Normalization •Gradient cross correlation	•Shape model	✓	0.84
[98]	2012		✓		50	•Cubic interpolation •neighbor interpolation	•Shape context registration •AAM	✓	0.81±0.12
[99]	2012	✓			NA		•3D AAM	✓	0.88±0.11
[100]	2016	✓			29	•Registration	•SRS	✓	0.89±0.02
[101]	2017	✓			21, 16	•Stick Filtering • Enhancement • Cropping	•FCM	✓	0.90±0.17

Dataset: Pv-Private, Pro-12-PROMISE12, NCI-13-NCI-ISBI-2013

developed a local ROI-specific atlas-based (LABS) technique, which generates a region of interest (ROI) in particular MRI slices to ensure better registration of atlas to target images for segmenting prostate WG and TZ. Chilali *et al.* [87] proposed zonal segmentation of prostate gland technique by registering a target image with atlas and then obtained the localization of the prostate zone by C-mean clustering technique. Yang *et al.* [88] performed 3D prostate MRI segmentation by local patch-based fusion of the atlas that was carried out using anatomical signature-based voxel weighting. The final segmentation of the prostate region is selected based on the majority voting rule.

B. MODEL-BASED PROSTATE MRI SEGMENTATION - RELATED PAPERS

A summary of 10 model-based whole gland (WG) prostate segmentation methods is tabulated in Table 2 covering the work from 2005 until 2016. The segmentation techiques was mostly developed on private datasets collected by the research institution and two publicly available dataset of PROMISE-12 and NCI-ISBI 2013. Zhu *et al.* [90] have introduced a 2D+3D hybrid network for better segmentation of the prostate MRI using 3D MRI data. Vikal *et al.* [91] performed 3D MRI volumes segmentation using a statistical appearance shape model (3DASM). The statistical shape model output is compared with the manual segmentation. Two different locally collected datasets having 33 and 15 MRI images are used to evaluate the algorithm. Gao *et al.* [92] developed an algorithm that registers the MR images to learn shape before segmenting the prostate gland. Makni *et al.* [93] developed a mathematical model of the statistical 3D shape model (SSM) [94], which can be deformed to match the contours of the prostate. Markov fields have also been used to collect knowledge about voxel neighborhoods. The iterative conditional mode algorithm estimates the final optimum labels based on Bayesian a posteriori classification. Chandra *et al.* [95], introduced a deformable model approach to segment the prostate gland, including seminal vesicles automatically. A deformable model trained on-the-fly and designed to be a model of patient-specific triangulated shape

and image attributes trained throughout its initialization. The image attribute model is integrated to deform the initialized shape by template matching image attributes (via normalized cross-correlation) to the scan characteristics. The resulting deformations are regularized over the shape via well-established simple shape smoothing algorithms, which are then made anatomically valid via an optimized shape model.

Toth and Madabhushi [96] developed the level-set segmentation method to make proper use of the gradient, intensity, statistical and geometric information to perform precise segmentation and localization of the prostate gland. Yin *et al.* [97] implemented an automated 3D MRI prostate segmentation method. Cross-correlation of the normalized gradient fields is used to detect the prostate displacement and size, and a graph search algorithm is then used to refine the boundaries. The experimental results of testing their methodology are calculated on a 551-image dataset. 3D ASM is less robust when volumetric data is sparse in one dimension. The data of 13 patients is utilized for testing the hybrid ASM network. Maan and van der Heijden [98] applied the shape context registration with active appearance model (AAM) to perform segmentation of 3D prostate T2W MRI. Shape context registration registers every training case to the segmented reference image. Then, the final segmentation is performed by an AAM. Ghose *et al.* [99] developed a 3D automatic segmentation of the prostate using multiple AAM with global registration for shape restriction. Shape and appearance information is derived by principal component analysis (PCA). The algorithm is evaluated on 15 MRI images. Khalvati *et al.* [100] performed segmentation of the prostate gland by registering the volume data against each other using sequential registration-based segmentation (SRS) algorithm.

Rundo *et al.* [101] developed a Fuzzy C-Means (FCM) clustering algorithm-based automatic prostate gland segmentation approach using multispectral T1-weighted (T1W) and T2-weighted (T2W) MRI images. The prostate gland was effectively segmented using this unsupervised machine learning technique.

In general, a fair comparison for the conventional methods of atlas-based and deformable-based segmentation cannot really be performed since most of the techniques use private datasets except for [87] and [98] that used PROMISE-12 dataset. The performance of both atlas-based [87] and deformable-based [98] WG segmentation is comparable in terms of DSC values, recorded at 0.817 and 0.81. The best performance for WG segmentation recorded by both methods using private dataset is at 0.90 for atlas-based [81] and 0.93 for deformable-based [91]

C. DEEP LEARNING-BASED PROSTATE SEGMENTATION LITERATURE WORK

After the breakthrough of deep learning, the deep convolutional neural network (DCNN) ia considered to be effective in semantic segmentation applications. The DCNN employed labelling to each pixel with a class of objects/non-objects. Semantic segmentation plays a significant role in the understanding of image which are essential for image analysis tasks. In general, the DL-based segmentation techniques can be groups in to 5 classes as illustrated in Figure 5. Details on the related papers being grouped according the 5 classes are presented in the subsequent sections.

1) FEATURE ENCODER-BASED PROSTATE MRI SEGMENTATION - RELATED PAPERS

A summary of papers on feature encoder-based segmentation techniques are listed in Table 3. The work can be either on segmentation or combination of segmentation and classification. The results for segmentation are presentation in DSC values whereas when segmentation is integrated into the prostate cancer detection framework, the results are reported in terms of accuracy.

Liao *et al.* [102] developed an unsupervised deep learning framework called independent subspace analysis (ISA) network. The ISA network extracts useful features from the input data. Subsequently, the extracted features are utilized by sparse label propagation to perform segmentation. Yanrong Guo *et al.* [103] has introduced a novel hybrid model by integrating a deformable model with stacked sparse auto-encoder (SSAE). The features extracted from deep learning are matched to the atlas by a sparse matching process. Cheng *et al.* [104] merged the supervised atlas-based active appearance model (AAM) with CNN. The method employed the volume of interest (VOI) created by AAM as an input to CNN model (appreciable features), which improved prostate segmentation accuracy.

Jia *et al.* [105] developed hybrid approach and probabilistic atlas are built by deformable registration via attribute matching and mutual-saliency weighting (DRAMMS) algorithm [106], and then patches are extracted from the selected atlas ROI to perform segmentation using ensemble DCNN network. Clark *et al.* [107] modified U-Net with inception residual blocks [108] to perform whole prostate gland (WG) and transitional zone (TZ) segmentation using DW MRI images. Mun *et al.* [109] developed baseline convolutional neural network (BCNN) with a residual feature for 3D MRI segmentation. All the blocks contain three layers of convolution, but there is a shortcut connection to sum the output of the first layer with the output of the second layer in the encoding blocks. There is no corresponding connection in the decoding part. The downsampling part extracted feature maps are reused in the upsampling part utilizing long connections and element-wise sum. The network managed the MRI slices as a data sequence to assist the segmentation process in the apex and base region. Brosch *et al.* [110] implemented a hybrid technique of convolutional neural network and shape-based model. Shape-based model utilizing 3D generalize through transformation (GHT) [111] to localize the boundary points of the prostate. CNN is applied to the output of the shape-based model to refine the segmentation of prostate MRI images. Karimi *et al.* [112] extracted

TABLE 3. Summary of the feature encoder-based prostate MRI segmentation, cancer detection techniques and their performance.

Paper No.	Year	Dataset					No of Images	Pre-processing Technique	Technique	Performance					DSC or Accuracy
		Pv	Pro 12	NCI ISBI	Pro Ex	Pro Ex2				WG	PZ	CG	TZ	ACC	
[102]	2013	✓					30	•Patch Extraction	•Stacked ISA	✓					0.867±0.02
[103]	2015	✓					66	Bias •Field Correction •Histogram Matching	•SSAE •Deformable model	✓					0.871±0.04
[104]	2016	✓					120	•Patch Extraction	•ANN •CNN	✓					0.925
[105]	2017	✓	✓				12, 50	•Reslicing •Normalization	•Atlas •DCNN	✓					0.91
[107]	2017	✓					104	•Manual segmentation • Data augmentation	•DCNN	✓			✓	✓	0.93, 0.88, 0.97
[109]	2017		✓				50	•Data augmentation	•BCNN	✓					0.86
[124]	2017	✓					172	•Bilinear interpolation	•Co-trained CNN					✓	0.903
[110]	2018		✓				50	• Data augmentation • Contrast enhancement	•CNN	✓					0.905±0.017
[112]	2018	✓	✓				49, 50	•Data augmentation •B-spline interpolation	•Shape model •CNN	✓					0.88
[113]	2018	✓			✓		360, 112	•Data augmentation •Cropping	•TDN •CNN	✓				✓	AUC=0.962
[114]	2018		✓				50	•Bias filed correction •Random deformation •Centre cropping	•DDSP ConNet	✓					0.857
[115]	2018				✓		112	•Normalization •Data augmentation	•Patch extraction •DCNN					✓	AUC=0.944
[116]	2019		✓	✓		✓	130, 10, 50	• N4 correction •Isotropic upsampling •Reorientation •Scaling	•HNN •Short Connection	✓		✓			0.92, 0.90
[119]	2019	✓					240	•Normalization •Data augmentation	•AlexNet	✓					0.95
[120]	2020				✓		112	Nil	3D CNN	✓					0.86±0.05
[121]	2020	✓					377	•Registration •Resampling •Cropping	•3D CNN	✓	✓				0.65, 0.89
[122]	2020	✓					330	•Data augmentation •Cropping	•3D CNN •Ellipsoid formula	✓			✓		0.871
[125]	2020	✓			✓		89, 50	•Linear Interpolation •Normalization •Cropping	•3D Multistream CNN	✓					0.925, 0.939

Dataset: Pv-Private, Pro-12-PROMISE12, Pro-Ex-PROSTATEx, Pro-Ex2-PROSTATEx2, NCI-13-NCI-ISBI-2013.

the information about the variable shape of the prostate by shape-based model and then applied CNN to refine the segmentation of prostate gland MRI images. Wang *et al.* [113] performed the detection of prostate cancer using a tissue deformation network (TDN) with CNN. The TDN provide method for registration of the mp-MRI modalities. The combination of both TDN and CNN extracts and classifies the features more accurately.

Liu *et al.* [114] developed a novel CNN technique called densely dilated spatial pooling convolutional network (DDSP ConNet) trained with benign loss function to perform segmentation of prostate MRI. The DDSP network combining atrous convolution with global pooling enhanced the segmentation performance of CNN. Song *et al.* [115] built a patch-based version of the DCNN model focused on a combination of multiparametric MRI (mp-MRI) data to differentiate between cancerous and noncancerous tissues.

Cheng *et al.* [116] implemented holistically nested net (HNN) with short connection to perform whole gland and central gland segmentation of prostate MRI images. Post processing was applied to refine the segmented images.

Liu *et al.* [117] created a new deep learning-based method for automatic prostate zone segmentation that includes a fully CNN with a novel feature pyramid attention mechanism. The proposed CNN, in particular, was made up of three sub-networks: an enhanced deep residual network (based on the ResNet50) [62], a pyramid function network with focus [118], and a decoder. The ResNet50 was used to deal with heterogeneous prostate anatomy by incorporating high-level semantic functionality, and the pyramid network with attention was used to collect details at multiple scales.

Abdelmaksoud *et al.* [119] developed a technique for automatic diagnosis of prostate cancer. The prostate gland segmentation is obtained using level set technique, which utilizes the nonnegative matrix factorization (NMF) approach for better feature extraction in localizing the prostate gland. Lastly, CNN is applied for classifying the cancerous and non-cancerous tissue in the ADC map. Eppendorf *et al.* [120] have introduced a deep learning approach for the quick deformable distribution of clinical target volume contours from pretreatment to fractional scans. The three different trained CNNs were evaluated with various loss functions, based on contour overlap, prediction of the deformation field, and a hybrid of the two. Arif *et al.* [121] developed a 3D CNN to segment and identified the prostate lesion in mp-MRI of low-risk patients. Lee *et al.* [122] developed 3D CNN of prostate T2W MRI for TZ and then compared the performance of segmentation with traditional volume measurements obtained with the ellipsoid formula [123].

Yang *et al.* [124] developed a novel CNN approach to automatically segment the prostate region and the lesion location in the prostate region in registered DWI and T2W MRI.

Based on Table 3 the performance of feature encoder-based segmentation using PROSTATEx for WG segmentation has the best DSC score at 0.925 [125]. The good performance of the method can be attributed to the architecture of multi-stream 3D CNN architecture that simultaneously processes anisotropic multi-planar MRI images; axial, sagittal

TABLE 4. Summary of the upsampling-based prostate MRI segmentation, cancer detection techniques and their performance.

Paper No.	Year	Dataset						No of Images	Pre-processing Technique	Technique	Performance					DSC or Accuracy
		Pv	Pro 12	NCI ISBI	I2 CVB	Pro Ex	Pro Ex2				WG	PZ	CG	TZ	ACC	
[153]	2016		✓					50	•B-spline interpolation •Histogram matching	•V-Net	✓					0.869
[126]	2018	✓						583	•Resampling •Cropping •Padding •Normalization	•3D FCN •Skip-connections					✓	0.903
[127]	2018	✓	✓					50	•Croping •Resizing •Normalization	•3D DM-net	✓				✓	0.890±3.09, 0.95±0.53
[131]	2018		✓	✓				60 , 50	•Windowed sinc interpolation	•PS-Net	✓					0.85
[151]	2018		✓					50		•3D U-Net	✓					0.921
[152]	2018	✓	✓	✓				53, 50, 60	•Data augmentation	•Aniso-3D U-Net		✓		✓		0.60, 0.85
[128]	2019	✓						26	Nil	•NMF •CNN					✓	0.93
[132]	2019		✓					50	•Data augmentation •Normalization	•FCNN	✓					0.873
[134]	2019				✓			19	•Cropping •Interpolation •Normalization	•U-Net		✓	✓			0.794, 0.692
[135]	2017	✓						1234	•Data augmentation	•U-Net	✓					0.885
[154]	2017		✓					50	•B-spline interpolation •Histogram matching •Data augmentation	•3D U-Net	✓					0.869
[136]	2019	✓						397	•Normalization •Cropping •Rigid transformation	•FL •MFL •SD-CRF	✓					0.573±0.1
[137]	2019		✓					50	•Denoising •Resizing	•Cascaded U-Net	✓					0.856
[138]	2019		✓					50	•Resizing	•3D FCN •SG	✓					0.91±0.2
[139]	2019				✓			19	•Normalization	•U-Net		✓	✓			0.587, 0.888
[140]	2019		✓					50	•Resizing	•Nested V-net3d •V-net2d	✓					0.92
[141]	2019				✓			19	•Rescaling	•FCN •LSTM	✓					0.86
[142]	2019					✓		991	•Data augmentation	•MDC •MPB	✓					0.88
[144]	2019								Nil	•3D/2D hybrid U-Net	✓					0.87
[145]	2019		✓					50	•Denoising •Resampling •Resizing	•Cascaded U-Net	✓					0.878
[146]	2019	✓		✓	✓			60, 19, 21	• Cropping	•USE-Net		✓	✓			0.76, 0.915
[133]	2019						✓	112	•Data augmentation	•ED-DenseNet	✓					0.871±0.06
[147]	2020	✓	✓					39, 50	•Data balancing •Resizing •Normalization	•2D U-Net	✓	✓				0.87, 0.89
[148]	2020		✓					50	•Normalization	•DCNN •Atlas	✓					0.848
[149]	2020		✓					50	•Standardization •Normalization	•AdaResU-Net	✓					0.849
[150]	2020		✓	✓				60, 50	•Resizing •Normalization •Nearest neighbor interpolation •Bilinear interpolation	•3D U-shaped	✓					0.91, 0.91

Dataset: Pv-Private, Pro-12-PROMISE12, Pro-Ex-PROSTATEx, Pro-Ex2-PROSTATEx2, QIN-P-QIN-PROSTATE-Repeatability, NCI-13-NCI-ISBI-2013, I2CVB-Initiative for Collaborative Computer Vision Benchmarking.

and coronal to produce a high-resolution prostate segmentation. The segmented outputs of all CNN are ensembled at the post-processing step. Training of the proposed network with triple-plane MRI images has enhanced the performance of prostate gland segmentation.

On the other hand, based on PROMISE-12, the best performance is reported by [116] with DSC for WG segmentation at 0.92. The method employs multiscale and multilevel learning, using 2-D nested networks with short connections for addressing the issue of ambiguity in segmentation of apex and base regions. In addition, post processing steps was applied to refine the segmented images.

2) UPSAMPLING-BASED PROSTATE MRI SEGMENTATION - RELATED PAPERS

A summary of upsampling-based prostate segmentation related papers from 2008 until 2020 is tabulated in Table 4. Here, segmentation performance are evaluated in terms of DSC values. For papers that implemented segmentation techniques for prostate cancer detection, their results are presented in the form of classification accuracy [126]–[128] and free-response receiver operating characteristics (FROC) [129].

In the paper by Mehrtash *et al.* [126] 3D FCN is developed with a skip connection for prostate MRI segmentation and localization of biopsy needles in MRI images. The encoder consists of a convolution layer with ReLu and max pooling layers to extract and save feature maps. To *et al.* [127] developed 3D deep dense multipath neural network (3D DM-Net), which employs DenseNet [130] in encoder network. The decoder network has residual blocks and grouped convolution, which help to produce the fine segmentation output. The validation of the model is performed on private as well as PROMISE-12 challenge datasets. Tain *et al.* [131] fine tuned the last layer of FCN and performed segmentation of prostate MRI using mp-MRI. Reda *et al.* [128] developed an automatic detection and localization technique of prostate cancer in DWI MRI. The level set model utilizes non negative matrix factorization (NMF) to combine the features intensity and shape information of prostate volume for accurate

segmentation. Then, feature maps are estimated at five values for the ADC map of the prostate regions.

In [132], Hassanzadeh *et al.* introduced a new segmentation technique based on eight different 3DFCN and structure of short connections to perform segmentation of prostate MRI images. Yuan *et al.* [133] developed a novel encoder-decoder densely connected convolutional network (ED-DenseNet). Dense residual connections are employed in between convolutional layers in the encoder and decoder network, and joint loss function is used in the decoder to evaluate network segmentation efficiency based on reconstruction and prediction error.

Jensen *et al.* [134] introduced U-Net based CNN for zonal prostate T2W MRI segmentation on z-score normalized data from two scanners, 1.5-T GE and 3-T Siemens. For segmentation of CG and PZ, the DSC is used for performance evaluation of the proposed CNN techniques. Zhu *et al.* [135] developed a deep encoder-decoder with additional supervised layers to perform the segmentation of prostate on MRI images. Yang *et al.* [124] developed a novel CNN approach to automatically segment the prostate region and the lesion location in the prostate region in registered DWI and T2W MRI.

Cao *et al.* [136] presented a CNN for prostate region segmentation and detection of lesions with focal loss and dense conditional random field (SD-CRF). Focal loss balances the classes and improved detection with post-processing and dense conditional random field (SD-CRF). Li *et al.* [137] developed dense U-Net for segmentation of prostate MRI. The output of the first U-Net is fed into the second U-Net to refine the segmentation.

Zhong *et al.* [138] developed a 3D fully convolutional network-Savitzky-Golay (FCN-SG) with long skip connection and the Parametric Rectified Linear Unit (PReLU) being the activation function. To further refine segmentation results, Savitzky-Golay (SG) filtering is employed as the post-processing step.

Huang *et al.* [139] implemented U-Net for segmentation of prostate cancer tissue in mp-MRI; Dynamic contrast-enhanced (DCE) and DWI MRI images. Öcal and Barisci [140] fused the Nested 3D dimensional volumetric convolutional neural network (Nested-Vnet3d) and 2D volumetric convolutional neural network (V-net2d) for segmentation of prostate trained and tested on PROMISE-12 challenge dataset. In [141], Kang *et al.* proposed a 3D segmentation technique using volumetric convolutional network and temporal stream modeled using recurrent neural networks with long short-term memory (LSTM) units. Ma *et al.* [142] modified the U-Net with multi-scale dilated convolution (MDC) and pooling block (MPB) to extract and encode multi-level features. The attention gate [143], along with adversarial loss, resulted in enhanced PZ segmentation.

Van *et al.* [144] implemented a hybrid 2D/3D deep learning approach to automatically locate and segment prostate organs on clinically acquired mp-MRI. In another work by Chen *et al.* [145], a cascaded Dense-U-Net is used for segmentation of prostate gland in three stages. In the first stage, Dense-U-Net is applied to acquire prostate gland segmentation for each MRI slice. In the 2nd stage, the morphological operation is applied to refine the segmented output. Lastly, the MRI slices containing the prostate region are resized to normalize the prostate region scale before feeding to Dense-U-Net for final segmentation.

Rundo *et al.* [146] introduced a new U-Net-based segmentation method called USE-Net, which uses blocks of Squeeze-and-Excitation (SE) in both the U-Net encoder and decoder architecture. The network was trained and tested on multi-dataset to generalize both intra-and cross-dataset. Their results revealed that the SE blocks allow recalibration of adaptive features, thus providing an excellent generalization of cross-datasets.

Astono *et al.* [147] implemented a simple 2D U-Net model for prostate segmentation based on a private dataset of T2 weighted MRI images with fixed 2D resolution and voxel size across the entire dataset.

Da Silva *et al.* [148] developed coarse segmentation that applies the intrinsic manifold simple linear iterative clustering algorithm and probabilistic atlas to combine local texture and spatial knowledge in a deep CNN model along with the particle swarm optimization algorithm to distinguish prostate and non-prostate tissues.

Baldeon-Calisto *et al.* [149] developed a novel technique called AdaResU-Net. Here, the U-Net with a residual learning framework is implemented, which has improved the segmentation of prostate in MRI images.

Zhou *et al.* [150] implemented a novel 3D U-shaped neural network for prostate gland MRI segmentation. The network has three key features: a resolution-aware convolutional downsampling layer, a residual instance-batch-normalization (IBN) block structure, and a case-wise loss function. Also, in the inference stage, a coarse-to-fine iterative segmentation is used to achieve high precision segmentation.

Meyer *et al.* [151] developed a 3D system for segmentation of prostate multiplanar MRI images. The multiplanar MRI improved the segmentation performance for the whole gland and also base and apex regions. The short and long residual convolution enhanced the prostate MRI segmentation accuracy, and the rank in the open challenge of PROMISE-12 dataset in 3D segmentation.

Mooij *et al.* [152] introduced aniso-3DU-Net for segmentation of anisotropy MRI volumes of prostate. Milletari *et al.* [153] performed the 3D segmentation of prostate gland MRI using volumetric CNN with a novel objective function.

Yu *et al.* [154] implemented residual connections within the 3DCNN to perform segmentation of prostate MRI volumes and evaluated the network using DSC, hausdorff distance (HD), average boundary distance (ABD) and relative absolute volumes difference (RVD).

Yuan *et al.* [133] developed a novel encoder-decoder densely connected convolutional network (ED-DenseNet). Dense residual connections are employed in between

TABLE 5. Summary of the resolution increment-based prostate MRI segmentation, cancer detection techniques and their performance.

Paper No.	Year	Dataset						No of Images	Pre-processing Technique	Technique	Performance				DSC or Accuracy
		Pv	Pro 12	NCI ISBI	I2 CVB	Pro Ex	QIN P				WG	PZ	CG	ACC	
[155]	2019	✓						15		•3D DSA-FCN	✓				0.852
[171]	2019	✓	✓					81,50	•Resampling •Random cropping •Normalization	•cascaded U-Net	✓				0.925
[157]	2019				✓			19	•Denoising • Cropping •Resizing	• DeepLabV3+ with Xception Model		✓	✓		0.70, .81
[158]	2019		✓					50	• Bias field correction •Data augmentation • Scaling	•HD-Net	✓				0.93
[159]	2019		✓	✓				60, 50	Resizing	•ResNet101 •DDSP	✓				0.95
[160]	2019			✓				60	•Resizing •Data augmentation	•Encoder-Decoder networks		✓	✓		0.732, 0.892
[162]	2019		✓					50	•Intensity mapping • Normalization •Resizing	•P-DNN	✓				0.841
[163]	2019		✓					50	•Resizing •Padding •Cutting	•Z-Net	✓				0.85
[164]	2019					✓		112	•Interpolation •Affine co-registration •Normalization	•CNN •SLM					AUC =0.54
[166]	2019	✓						566	•Data augmentation	•Modified U-Net	✓	✓			0.89±0.01, 0.86±0.01
[167]	2019			✓				19	•N4Bias correction technique •Histogram normalization	•3D U-Net	✓	✓		✓	0.799, 0.855, 0.908, 0.920
[168]	2019	✓						50	•Resampling •Trilinear interpolation •Intensity Cliping •Scaling	•3D CNN	✓				0.60±1.7
[169]	2019	✓						346	•Randomly sampling •Patch extraction •Data augmentation	•ResNet	✓			✓	0.71, 0.93
[170]	2019		✓					50	•Normalization	•3D dilated U-Nets	✓				0.88±0.4
[171]	2019	✓	✓					81,50	•Resampling •Random cropping •Normalization	•BOWDANet	✓				0.925
[129]	2019	✓						417	•Registration •Normalization •Variation	•Deeplab •FocalNet •U-Net					FROC=0.897, 0.879
[161]	2019	✓						232	•Normalization	•Adapted U-Net	✓				0.89±0.03
[156]	2019	✓						163	•Cropping	•Cascaded U-Net	✓	✓			0.927±0.04, 0.793±0.10
[172]	2020	✓	✓	✓				50, 60, 32	•Resizing	•MDP •DDPG	✓				0.936
[173]	2020			✓				60	•Resizing •Cropping •Normalization •Data augmentation •2D patches	•DeepLabV3+	✓	✓	✓		0.789, 0.928, 0.919
[174]	2020		✓	✓	✓			50, 60,19	•Resizing •Normalization	•SAML	✓				0.876
[175]	2020		✓					50	•Normalization	•V-net Light (VnL)	✓				0.86
[176]	2020						✓	15	•3D affine transformation	•Chan-vese active contour	✓				0.907
[177]	2020		✓	✓				60,50	•Data Augmentation	•CDA-Net	✓				0.928, 0.926
[178]	2020	✓						50	•Denoising •Normalization	•Supervise U-Net	✓				0.895
[179]	2020	✓		✓				202, 60	•Normalization •Biase field correction •Data augmentation •Cropping	•3D Multistream Network •PAM •RRB		✓	✓		0.785, 0.908, 0.806, 0.901
[180]	2020			✓	✓			60, 19	•Centre cropping •Normalization	MS-Net	✓	✓	✓		0.915, 0.912, 0.921
[181]	2020			✓				112	•Bias correction •Resampling •Normalization	•3D U-Net	✓	✓	✓		0.893, 0.825, 0.79, 0.788

Dataset: Pv-Private, Pro-12-PROMISE12, Pro-Ex-PROSTATEx, QIN-P-QIN-PROSTATE-Repeatability, NCI-13-NCI-ISBI-2013, I2CVB-Initiative for Collaborative Computer Vision Benchmarking.

convolutional layers in the encoder and decoder network, and joint loss function is used in the decoder to evaluate network segmentation efficiency based on reconstruction and prediction error.

3) RESOLUTION INCREMENT-BASED PROSTATE MRI SEGMENTATION - RELATED PAPERS

A summary of papers on resolution increment-based segmentation techniques are listed in Table 5. Majority of the papers reported results on segmentation of prostate except for two papers, [129], [155] which have proposed detection of prostate cancer by integrating segmentation techniques in their classification framework. Here, the results is expressed in terms of area under the ROC curve (AUC) and FROC.

In the paper by Wang *et al.* [156] novel technique called deeply supervised FCN is developed with concatenated atrous convolution (3D DSA-FCN) for segmentation of prostate volumes. Concatenated atrous convolution gathers multi-scale contextual information which improves localization of the prostate. In another paper by Zhu *et al.* [157], coarse segmentation of DWI MRI images is obtained by using morphological methods and watershed transform. The output of coarse segmentation is used to acquire the region of interest (ROI). The ROI is resized to 192 × 192 and then fed into a cascaded U-Net architecture for zonal segmentation of prostate MRI images.

Khan *et al.* [158] implemented DeepLabV3+ with Xception network is a backbone to perform an automatic zonal

segmentation for T2W prostate MR images of two different MRI scanners. The deep networks is trained with Dice loss function which performed better in terms of zonal segmentation using depth separable convolutions.

Jia *et al.* [159] developed a novel technique called hybrid discriminative network (HD-Net). The pyramid convolution block and the residual refinement block are implemented in HD-Net to collect multi-scale spatial contextual information of the prostate region. Later, the multi-scale features are combined to minimize the propagation loss.

In [160], Geng *et al.* introduced an encoder-decoder network with large receptive field to gather broader context using dense dilated pyramid pooling (DDSP) and the resampling of features at different scales provide more accurate classification of an arbitrary scale area.

DeepLabV3+ network with backbone ResNet18 [62] is implemented by Khan *et al.* [161] for zonal segmentation of prostate MRI using NCI-ISBI2013 dataset. In [162] Ghavami *et al.* evaluated six different deep convolutional neural networks for segmentation of prostate T2W MRI images. Yan *et al.* [163] has developed a network called propagation deep neural network (P-DNN) to combine multi-level features as a single model. The P-DNN network utilized the convolution and pooling layers (CP-layer) to extract high-level features to accurately identify the prostate position and shape identification. The output of CP-layer is refined in the propagation layer (P-layer), while the loss-layer (L-layer) correlates between the network output and manual segmentation. Zhang *et al.* [164] developed a novel technique called Z-Net. The novel approach is dense, having more layers that preserve more information to segment the prostate boundary better than the U-Net [67].

Lapa *et al.* [155] developed a convolutional neural network by replacing backpropagation with semantic learning machine (SLM) neuroevolution algorithm. The SLM network enhanced the prostate MRI images segmentation performance compared to XmasNet [165] for the PROSTATEx challenge dataset. Motamed *et al.* [166] introduced a transfer learning technique to perform the whole gland and transition zone segmentation by implementing a modified U-Net and loss function. In [167], Alkadi *et al.* performed the zonal segmentation and detection of PZ and CG by applying a 3D encoder-decoder convolutional neural network.

Zaffino *et al.* [168] developed a convolutional neural network for the automatic segmentation of multiple closely spaced brachytherapy catheters in intraoperative MRI.

In [169], Xu *et al.* performed segmentation of prostrate by implementing a ResNet network. The features are utilized in the training of residual networks for better segmentation of prostate lesions. Pan *et al.* [170] developed a two-stage 3D dilated model based on 3D dilated U-Nets with post-processing for the segmentation of prostate MRI. The method first localize the prostate followed by segmentation for better prostate segmentation. Cao *et al.* [129] have developed a multi-class CNN tool, FocalNet, for the identification of prostate cancer in mp-MRI. Gleason score (GS) is used to assess the level of aggressiveness of the prostate lesions hence allowing the FocalNet to collect enough information for good assessment of the lesion.

In [171], Zhu *et al.* developed a novel network called boundary-weighted domain adaptive neural network (BOWDA-Net) to solve the issue of intricate edges and variable anatomical structure of prostate MRI images. Advanced transfer learning helped the BOWDA-Net to address the issue of small number of MRI slices, and boundary loss function helped in giving precise boundary segmentation of prostate in MRI images. [172], proposed segmentation of prostate MRI is to be computed as a Markov decision process which is based on deep reinforcement learning (DRL) algorithm. The agent is trained by deep deterministic policy gradient (DDPG) to localize the region of interest (ROI) in prostate MRI images in multistep manner. Khan *et al.* [173] evaluated encoder-decoder network for segmentation prostate and its zone. The images of the dataset are centre cropped, normalized, and 2D patches are extracted to achieve better segmentation.

Liu *et al.* [174] have presented a novel shape-aware meta-learning scheme (SAML) for segmentation of the medical images. The SAML approach roots in the episodic training technique of meta-learning, to facilitate robust optimization by simulating the domain change during model training with meta-train and meta-test sets. Besides, two shape-aware loss functions have been used to regularize the meta optimization process. Yaniv *et al.* [175] modified the V-Net [153] network by replacing 3D convolutions with novel 3D Light modules. The new network depreciates the number of parameters without affecting the segmentation results. Singh *et al.* [176] implemented atlas-based method, along with partial volume (PV) correction algorithm to segment the PZ and TZ of the prostate. Finally, an active contour model of 3D Chan-Vase with morphological operations is utilized to obtain the final area of the prostate.

Lu *et al.* [177] developed a cascaded dual attention network (CDA-Net) for segmentation of prostate MRI scan. The CDA-Net extracts the region of interest (ROI) by applying RAS-Faster RCNN, and then multi-scale features are utilized by applying a residual convolutional block and soft-attention mechanism (RAU-Net) to locate the targeted region precisely. Hambarde *et al.* [178] implemented a deeply supervised U-Net network with radiomic features. A large number of radiomic features are extracted by the proposed network to locate the prostate gland precisely. Qin *et al.* [179] proposed a 3D multi-scale discriminative network with pyramid attention module (PAM) and residual refinement block (RRB) for zonal segmentation of prostate MRI bi-parametric images. The class imbalance issue is resolved by multi-directional edge loss which is a wavelet decomposition-based method, and PAM is utilized to extract the multi-scale discriminative features.

Liu *et al.* [180] have introduced a new network called the multi-site network (MS-Net), which have improved the prostate segmentation by learning generic representations

TABLE 6. Summary of the regional proposal-based prostate MRI whole gland (WG) segmentation, cancer detection techniques and their performance.

Paper No.	Year	Dataset			No of Images	Pre-processing Technique	Technique	Performance	DSC or Accuracy
		Pv	Pro Ex	Pro Ex2				WG	
[182]	2018	✓			80	•Resizing	•UR-Net	✓	0.936
[183]	2019	✓			78	•Resizing •Normalization	•Mask RCNN	✓	0.87
[184]	2020	✓		✓	120, 42	•Resizing •Bi-linear interpolation •Normalization	•Mask RCNN	✓	0.82±0.05
[185]	2020		✓		344	• Z-score normalization • Image registration •Cube interpolation	•CRF-RNN •XmasNet	✓	AUROC= 0.615

Dataset: Pv-Private, Pro-Ex-PROSTATEx, Pro-Ex2-PROSTATEx2.

from multi-site data. The MS-Net utilized the domain-specific batch normalization (DSBN) layer in the network backbone to counterbalance the inter-site data heterogeneity and learned high-level information from multi-site data.

In [162] Ghavami *et al.* evaluated six different deep convolutional neural networks for segmentation of prostate T2W MRI images. In another paper by Zhu *et al.* [157], coarse segmentation of DWI MRI images is obtained by using morphological methods and watershed transform. The output of coarse segmentation is used to acquire the region of interest (ROI). The ROI is resized to 192×192 and then fed into a cascaded U-Net architecture for zonal segmentation of prostate MRI images.

Zavala-Romero *et al.* [181] introduced a 3D multi stream U-Net for zonal segmentation of prostate MRI images. Moreover, the images of the dataset are normalized, and linear interpolation is used to the uniform resolution of MRI slices. The preprocessing of the dataset has enhanced the segmentation of the prostate MRI images.

From Table 4 and Table 5, it is clear that the upsampling-based method [127] and the resolution increment-based method [160] have recorded the best DSC score of 0.95 using the PROMISE-12 dataset, which is the highest DSC value recorded for a common dataset.

4) REGIONAL PROPOSAL-BASED PROSTATE MRI SEGMENTATION - RELATED PAPERS

The list of papers on regional proposal-based segmentation techniques, mainly segmenting the WG region, is presented in Table 6. In the work by Zhu *et al.* [182] a network called UR-Net is developed by implementing the U-Net in a combination with a recurrent neural network (RNN) layer. Feldman *et al.* [183] implemented Mask-RCNN for segmentation and localization of the prostate and the dominant intraprostatic lesion (DIL) on multiparametric ADC and T2W MRI (mp-MRI) images. Dai *et al.* [184] proposed segmentation of prostate and intraprostatic lesions (ILs) using mask region convolutional neural networks (Mask RCNN). T2W MRI images are utilized for segmentation of prostate, and for intraprostatic lesions (ILs) segmentation, the combination of apparent diffusion coefficient (ADC) and T2W MRI images are used. After re-sampling using bi-linear interpolation, the ADC map is rigidly registered to the T2W MRI.

To improve the classification efficiency of XmasNet, Lapa *et al.* [185] applied Conditional Random Fields as a Recurrent Neural Network (CRF-RNN) with a Convolutional Neural Network (CNN) architecture to the PROSTATEx17 Challenge dataset. Therefore, without the need for two separate training procedures, the proposed method creates CRF-XmasNet, a hybrid end-to-end trainable network composed of an initial CNN component for feature extraction and a CRF-based probabilistic graphical model component for organised prediction. Experimental tests show that the approach show improvement in terms of classification accuracy and training time. The results are reported in terms of statistical significant of different architectures with/without embedding the CRF-RNN and the very deep networks of VGG16 and AlexNet.

Limited works are using the regional proposal-based segmentation which has recorded the best DSC score of 0.936 with private dataset by the 2020 work of Zhu *et al.* [182]. Based on PROSTATEx2, its performance for WG segmentation of 0.88 DSC score but this is far less than the feature encoder-based method which was proposed in 2019 that achieved 0.92 DSC score [116].

5) GENERATIVE ADVERSARIAL NETWORK (GAN)-BASED PROSTATE MRI SEGMENTATION - RELATED PAPER

The list of papers on prostate segmentation based on GAN is presented in Table 7. Generative adversarial network [186] implements a generator network as a neural network that takes a random variable as input and applies a transformation function to generate similar distribution data as in the target distribution. In contrast, the second network, called discriminator, distinguishes the difference between the distribution of generated data and if real data — both networks work as adversaries.

Kohl *et al.* [187] proposed an approach by implementing FCN with adversarial training. The prostate cancer region is better detected by using adversarial loss in the segmentation CNN network. Jia *et al.* [188] proposed a 3D adversarial pyramid anisotropic network (3D APA-Net). The network applies 3D ResNet [62] to perform volumetric segmentation, and then GAN is utilized to refine the segmentation. The proposed method is tested on the online dataset: PROMISE-12 and NCI-ISBI 2013 dataset, respectively. Zhang *et al.* [189] developed Bi-attention adversarial network for prostate cancer segmentation. The generator network generates the predicted input image mask using U-Net as the backbone. The generator efficiency increases more

TABLE 7. Summary of the GAN-based prostate MRI segmentation techniques and their performance.

Paper No.	Year	Dataset			No of Images	Pre-processing Technique	Technique	Performance				DSC or Accuracy
		Pv	Pro 12	NCI ISBI				WG	PZ	CG	AC	
[187]	2017	✓			152	•Upsampling •Registration	•FCN •GAN	✓				0.41 ± 0.28
[189]	2019	✓			120	•Data augmentation	•GAN				✓	0.864
[190]	2019	✓			50	•Denoising	•cGAN	✓	✓	✓		0.734±0.18, 0.778±0.15, 0.742±0.16
[191]	2020	✓	✓		50	•Resizing	•U-Net •NSGAN •Difficulty-aware •Attention mechanism	✓				0.909±0.02, 0.901±0.01
[192]	2019	✓			60	•Normalization •Resizing •Centre cropping	•DGMNet	✓				0.93±0.12
[188]	2019		✓	✓	50, 60	•Bias field correction •standardization	•3D-APA-Net	✓	✓	✓		0.894±0.1, 0.864±0.02, 0.860±0.01
[196]	2020		✓		99, 50	•Resizing •Data augmentation	•SegDGAN	✓				0.925, 0.889
[195]	2020	✓	✓		60	•Scaling •Zero padding •Data augmentation	•U-Net •CycleGAN •cGAN	✓				0.76±0.10, 0.73±0.20, 0.789±0.12, 0.72±0.03, 0.70±0.03, 0.757±0.02
[16]	2020		✓		50		•cGAN	✓				0.889

Dataset: Pv-Private, Pro-12-PROMISE12, NCI-13-NCI-ISBI-2013.

by distinguishing the generator expected mask and the true mask with a discriminator network with adversarial learning. Grall *et al.* [190] implemented conditional Generative Adversarial Network (cGAN) for the segmentation of prostate MRI. The trained network is evaluated by adding noise from the training data to the test data. Finally, post-processing is performed to refine the output of the segmentation.

Nie *et al.* [191] developed a framework for prostate MRI segmentation. The developed framework consists of a segmentation network, confidence network, and difficulty aware attenuation mechanism. The confidence network generates a confidence map to provide information about the segmented region. Difficulty aware attenuation mechanism improves the segmentation process by injecting confidence learning with adversarial learning. Girum *et al.* [192] developed a novel technique called deep generative model neural network (DGMNet) for the segmentation of prostate MRI. Jia *et al.* [193] performed the efficient segmentation of prostate MRI by implementing a 3D global encoder-decoder network with an adversarial network. Multi-level hybrid global convolution blocks and boundary refinement blocks are used in the decoder part of the network. Hu *et al.* [194] developed a novel GAN called prostateGAN. The author combines the idea of DCGAN and cGAN to generate prostate DW MRI images with a specified glean score. The network is trained with a dataset of 104 patients having a 1490 prostate DW MRI slice. The 3D convolutional layer, along with the adversarial loss function, achieved prostate gland better localization and classification.

Cem Birbiri *et al.* [195] evaluated the cGAN, Cycle GAN and U-Net for the segmentation of prostate T2W MRI. Among the evaluated networks, the cGAN performed very well in terms of DSC for the mp-MRI dataset. Jun He *et al.* [16] implemented the conditional GAN (cGAN) with adversarial loss and feature matching loss for the segmentation of prostate MRI. During the training of cGAN, the high-level information is learned by the adversarial training, while multi-scale discrimination refined the prostate boundary.

From Table 7, the GAN-based prostate segmentation started to gain popularity in 2017 and its best performance using PROMISE-12 is by SegDGAN at 0.925 DSC score for WG segmentation [196]. The proposed method comprises a fully convolutional generative network of densely connected blocks and a discriminative network with multi-scale feature extraction. Notably, the method employed the mean absolute error and the Dice coefficient for optimized objective function, giving improved segmentation accuracy.

VII. THE IMPACT OF MULTIPARAMETRIC MRI

In clinical practises, it is important to utilize various imaging modalities for accurate prostate segmentation. One of every five cancer diagnoses is a prostate cancer [197] Traditionally, prostate cancer is diagnosed by biopsy but there is evidence of an unequivocal benefit of multiparametric MRI-targeted biopsies for more systematic biopsies in diagnosis of prostate cancer.

As the biopsy is planned, prostate MRI scanning helps in locating the target area, and therefore reduces the number of unnecessary biopsies by half, minimises over-diagnosis of clinically insignificant prostate cancer, and increases the identification of clinically meaningful prostate cancer [198]. T2W MRI has good resolution and contrast are preferred to be utilized for the staging and localization of prostate cancer. In zonal segmentation the diagnosis of prostate cancer is challenging in CG because of the difficulty in differentiating between normal and malignant tissue with low-SI. The DW MRI measures the movement of water molecules in the soft tissue of the prostate gland.

For better contrast of prostate tissue, DCE MRI is used since it exploits the vascularity characteristic of tissues [199]. Prior to scanning the DCE MRI, intravenous contrast media, normally gadolinium-based, is inserted into the patient. In comparison to T2-W MRI alone, DCE MRI with

TABLE 8. Summary of the mp-MRI prostate segmentation techniques and their performance.

Paper No.	Year	Dataset					No of Images	Pre-processing Technique	Technique	Performance				DSC or Accuracy
		Pv	Pro 12	I2 CVB	Pro Ex	MRI Modality				WG	PZ	CG	ACC	
[101]	2017	✓				T1W, T2W	21, 16	•Stick Filtering •Enhancement • Cropping	**(Deformable)** •FCM	✓			✓	0.90±0.17
[113]	2018	✓			✓	T2W, ADC	360, 112	•Data augmentation •Cropping	**(Feature Encoder)** •TDN •CNN	✓			✓	AUC=0.962±0.0107
[139]	2019			✓		T2W,ADC	19	•Normalization	**(Upsampling)** •U-Net		✓	✓		0.91±0.375
[183]	2019	✓				T2W, ADC	78	•Resizing •Normalization	**(Regional Proposal)** •Mask RCNN	✓				0.87±0.04
[195]	2020	✓	✓			T2W, DWI, ADC	60	•Scaling •Zero padding •Data augmentation	**(GAN)** •U-Net •CycleGAN •cGAN	✓				0.76±0.10, 0.73±0.20, 0.789±0.12, 0.72±0.03, 0.70±0.03, 0.757±0.02
[185]	2020				✓	T2W, ADC, PDW	344	• Z score Normalization • Image Registration •Cube Interpolation	**(Regional Proposal)** •CRF-RNN •XmasNet	✓				AUROC=0.615

Dataset: Pv-Private, Pro-12-PROMISE12, Pro-Ex-PROSTATEx,
I2CVB-Initiative for Collaborative Computer Vision Benchmarking.

T2-W MRI has shown to improve sensitivity of prostate cancer detection. Furthermore, the use of magnetic resonance spectroscopy (MRSI) in conjunction with MRI has shown to improve identification and diagnosis of prostate cancer [200].

Images from various MRI modalities reveal a great deal of variation between patients' prostate glands. The prostate organ may appear in various locations in images, and the signal intensity may be distorted during the acquisition process by noise or artefacts.

Computerized image interpretation systems are being developed to aid in assessment of prostate mp-MRI images, and their relationship between imaging and pathologic assessment [201]. A list of mp-MRI prostate segmentation and prostate cancer detection is given in Table 8. Rundo *et al.* [101] deformable model Fuzzy C-means clustering technique to perform the segmentation of prostate mp-MRI, T1W and T2W that is driven only by an image appearance model. Wang *et al.* [113] implemented the tissue deformation network (TDN) and CNN concatenated together to perform the detection of prostate cancer in mp-MRI. In short, the TDN is for automated prostate detection and registration of T2W and ADC whereas the dual-path CNN is for clinically significant (CS) prostate cancer detection. Huang *et al.* [139] developed U-Net based network for segmentation of prostate cancer region in mp-MRI. The mp-MRI of T2W and ADC has enhanced the localization of prostate cancer in mp-MRI images. Feldman *et al.* [183] performed better segmentation and localization of the prostate and the dominant intraprostatic lesion (DIL) on multiparametric ADC and T2W MRI (mp-MRI) images using Mask-RCNN. In [116] a trained deep neural network is utilized to extract features from mp-MRI and used it for segmentation of WG and CG yielding DSC equal to 0.92 and 0.90, respectively. Cem Birbiri *et al.* [195] evaluated different deep neural networks (cGAN, Cycle GAN and U-Net) for the segmentation of prostate mp-MRI dataset. The DSC values for [195] in Table 8 are listed for 3 GAN-based deep neural networks for private and PROMISE-12 datasets. Lapa *et al.* [185] performed the prostate cancer detection using 3 mp-MRI modality; T2W, ADC and proton density weighted (PDW) utilizing a hybrid network of CRF-RNN and CNN. The AUROC value in Table 8 is listed for the best model which is CRG-VGG16 model. Armato *et al.* [202] used multiparametric magnetic resonance images of PROSTATEx Challenge and PROSTATEx-2 Challenge to perform computerised classification of clinically relevant prostate lesions and computerised evaluation of Gleason Grade Group in prostate cancer. In the task of detecting clinically important prostate cancers, computer-aided diagnosis (CAD) algorithm using mp-MRI is shown to increase sensitivity but it decreases specificity, giving more false positives [203]. The lack of a public mp-MRI dataset of the prostate with well-defined performance indicators to compare mp-MRI CAD systems has been a major roadblock to development.

VIII. OVERVIEW OF CLINICAL APPLICATION OF DEEP LEARNING FOR PROSTATE MRI SEGMENTATION AND CANCER DETECTION

Development of computer-aided diagnosis (CAD) algorithms has been an active research field among the medical image processing community. In particular, the clinically useful algorithms are developed to assist clinicians, as decision support in diagnosis of prostate cancer and reducing unnecessary biopsies. In fact, prostate MRI is known to reduce unnecessary biopsies by 25%, reduce over-diagnosis of clinically insignificant prostate cancer, and improve detection of clinically significant cancer, which is defined as the one with biopsy Gleason score greater than 7 [204], [205]. This has motivated 3 grand challenges, PROMISE12 on prostate MRI segmentation [206] and PROSTATEx and PROSTATEx-2 on prostate cancer detection. Besides, the competitions promote discussion on the clinical implication of the proposed methods and facilitate direct comparison of the proposed algorithm. The subsequent discussion focuses mainly on the PROSTATEx and PROSTATEx-2 challenge due to its clinical motivation and involvement.

Using mp-MRI, the two tasks to be completed in the PROSTATEx and PROSTATEx-2 competitions are

(1) classification of clinically significant prostate lesions and (2) determination of Gleason Grade Group in prostate cancer. A thorough analysis on the results PROSTATEx and PROSTATEx-2 Challenge is provided by Armato *et al.* [202]. The results from PROSTATEx Challenges are in agreement with clinical practice with the highest AUC value of 0.95 indicating the great potential of the proposed method in reducing the number of unnecessary biopsies. The PROSTATEx-2 Challenge demonstrates that classification of 5-class pathologic Gleason Grade Group is a more difficult task than to discriminate between clinically significant and clinically insignificant cancer regions. From a clinical perspective, the focus of the algorithm development should be on discriminating between low- and high-grade cancers so that the number of biopsies can be reduced.

A. COMMON PROBLEMS IN PROSTATE MRI SEGMENTATION

Data scarcity is the main limitation in the segmentation of medical images via DCNN, usually leading to over-fitting, which refers to a model that performs well on a training dataset but does not perform well on new data. In the majority, medical image analysis tasks, sufficient dataset with concerned masks are not available for training of DCNN because the dataset delineation is time-consuming and sometimes prone to error due to less number of experts in this field. Special care must be taken during DCNN training with limited images to prevent over-fitting. Consequently, by reducing the layers or parameters, the complexity of DCNN can be reduced or, without changing the network architecture, focus on methods that artificially augment [207], [208] the training data.

1) CLASS IMBALANCE

The region of interest in prostate MRI occupies a small region, which causes the issue of class imbalance. The main challenges of prostate MRI segmentation are addressing imbalanced data. Class imbalanced data can lead to unstable DCNN training for prostate MRI segmentation, which is biased towards the larger-region class. The loss function can be used as a systematic way to improve the low dominant class, improve the learning process, and avoid being trapped in local minima. In order to overcome the imbalance class present in the data collection, larger weights are allocated for labels with fewer total pixels and smaller weights for labels with more total pixels. Loss functions are one of the primary ingredients in methods for deep learning-based segmentation of medical images. More than 20 loss functions for various segmentation tasks have been proposed in the past four years where mostly used for segmentation process [209].

a: LOSS FUNCTION

Five different types of loss functions are elaborated in this article, which are used in prostate MRI images segmentation as summarized in Figure 6.

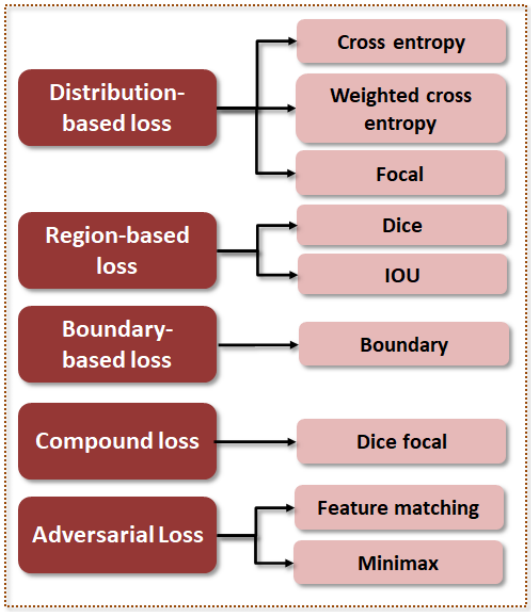

FIGURE 6. 5 classes of loss functions and its sub classes used for development of deep learning-based prostate MRI segmentation.

b: DISTRIBUTION-BASED LOSS

2) CROSS-ENTROPY (CE) LOSS

The most widely used loss function for image segmentation tasks is the cross-entropy loss. The cross-entropy loss tests the class predictions for each pixel vector separately and then combines all pixels. The imbalanced classes weight in images might affect the classifier decision.

In Long *et al.* [66] applied CE loss to address the issue of class imbalance. Mathematically, CE can be calculated as

$$Loss_{CE} = -\sum_{i\varepsilon N}\sum_{i\varepsilon L} y_i^l, \log\hat{y}_i^l, \tag{4}$$

where $\hat{y}_i^l$ predicted segmentation class, y_i^l is the target or the ground truth segmentation label, N is the set of all target labels, and L is the set of all labels.

3) WEIGHTED CROSS ENTROPY (WCE) LOSS

In prostate MRI scan, background regions dominate the remaining classes. Therefore, the weights of multiple classes are included in the cross-entropy as follows [173], [207].

$$Loss_{WCE} = -\sum_{i\varepsilon N}\sum_{i\varepsilon L} w_i y_i^l \log\hat{y}_i^l, \tag{5}$$

where $\hat{y}_i^l$ predicted segmentation class, y_i^l is the target or the ground truth segmentation label and w_i represents the weight assigned to the $i-th$ label.

4) FOCAL LOSS (FL)

Originally, focal loss was introduced for the task of detection. The focal loss encourages the model to down-weight and concentrates training on hard negatives [210]. Formally,

the FL is described by adding a modulating factor for the loss of cross-entropy and a class balance parameter,

$$Loss_{FL}(P_t) = -\alpha t(1-P_t)^{\gamma}\log(P_t), \tag{6}$$

where $p_t \in (-1,+1)$ is the estimated probability for the class. The γ is a parameter which smoothly adjusts the rate of weight and setting $\gamma > 0$ can reduce the relative loss of classified samples. It should be noted that the focal loss is equal to the original cross-entropy loss when $\gamma = 0$.

a: REGION-BASED LOSS

The goal of regional loss functions is to minimize the incompatibility or maximize the overlap between ground truth and predicted segmentation regions.

5) DICE LOSS (DSL)

For medical image segmentation, the common loss function is Dice loss, which measures the difference between the sample predicted and the actual sample [153]. The Dice loss scale from 0 to 1 and the maximum Dice overlap value is 1.

$$Loss_{DSL} = 1 - \frac{2\sum_{i=1}^{N}\hat{y}_i y_i}{\sum_{i=1}^{N}\hat{y}_i^2 + \sum_{i=1}^{N} y_i^2}, \tag{7}$$

where the sum run over all test images, $\hat{y}_i$ is the predicted segmentation class and y_i is the target or the ground truth segmentation label.

6) INTERSECTION OVER UNION LOSS (IOU) LOSS

IoU loss [211] is similar to Dice loss and designed for optimization of segmentation metrics.

$$Loss_{IOU} = 1 - \frac{y \bigcap \hat{y}}{y \bigcup \hat{y}} + R(y,\hat{y}), \tag{8}$$

where $R(y,\hat{y})$ is the penalty term for predicted segmentation class $\hat{y}$ and the ground truth segmentation label y.

a: BOUNDARY-BASED LOSS

Boundary-based loss is aimed at reducing the difference between ground truth and segmentation image. In general, boundary-based loss functions are used with a region-based loss to achieve more robust training.

7) BOUNDARY-BASED LOSS (BL)

In order to calculate the distance between two boundaries differently, boundary losses use integrals across boundaries rather than unbalanced integrals across regions to mitigate the difficulty of a highly unbalanced region [212], [213].

$$Loss_{BL} = \int_{\Omega} \phi G(p) s_{\theta}(p) dp, \tag{9}$$

where $p \in \Omega$ is a point on boundary G. The level set function $\phi G(p)$ encodes the distance between each point q, and softmax probability outputs of the network $s_{\theta}(p)$.

a: COMPOUND LOSS

Compound loss function applied to the prostate segmentation applications is described as follows:

8) DICE FOCAL LOSS

The Dice Focal loss function is a combination Dice and focal loss to be minimized the loss during the segmentation of small volumes [214].

$$Loss_{DF} = C - \sum_{c=0}^{C-1} \frac{TP_p(c)}{TP_p(c) + \alpha FN_p(c) + \beta FP_p(c)} - \lambda \frac{1}{N} \sum_{c=0}^{C-1}\sum_{n=1}^{N} g_n(c)(1-p_n(c))^2 log(p_n(c)), \tag{10}$$

where $TP_p(c)$, $FN_p(c)$ and $FP_p(c)$ are the true positives, false negatives and false positives for class c, respectively, determined by the predictive probabilities. Here, $p_n(c)$ is the expected likelihood for voxel n being class c, $g_n(c)$ is the ground truth for voxel n being class c, C is the total number of classes. The trade-off between Dice loss and focal loss is λ, α and β are the trade-offs of penalties for false negatives and false positives, N shows the total number of the voxel.

a: ADVERSARIAL LOSS

9) FEATURE MATCHING LOSS

The feature matching loss function [215] is applied to regularise the GAN generator and prevent it from over training the discriminator. The generator is trained to produce features that fit the expected values. In addition, the discriminator selects those features that are most selective between the actual data and the generated data. The feature matching loss function of a network, E is

$$F(x) = min_{\theta} \sum j = 1^{M} \left\| E_x \sim p_{data} E_j(x) - E_z \right\| \sim N(0, I_{nz}) E_j(G(z;\theta)) \right\|^2, \tag{11}$$

where x is the real data sample from the data distribution p_{data}, z is a noise vector, $E_j(x)$ is the output feature map of the hidden layer j and $N(0, I_{nz})$ is the normal distribution of data.

10) MINIMAX LOSS

In GAN, the generator network try to minimize the objective function $F(x)$, while the discriminator try to maximize the function.

$$F(x) = min_g max_d [E_x \sim p_{data}[log(D_d(x)) + E_z \sim p_{(z)}[log(1 - D_d(G_g(z)))] \tag{12}$$

where E_x is the expected value over all real data instances, $D_d(x)$ is the discriminator's estimate of the probability that data instance x is real, $G_g(z)$ is the generator output when

TABLE 9. Summary of publicly available MRI dataset for prostate segmentation and prostate cancer (CaP) detection.

Dataset Name	Year	MRI Modality				Ground Truth Label	No. of Images(i) / Subjects(s)
		T2W	DWI	DCE	ADC		
PROMISE12	2012	✓				WG	50 (s)
NCI-ISBI-2013	2017	✓				WG, CG, PZ	60 (s)
I2CVB	2015	✓	✓	✓	✓	WG,CG,PZ, CaP	19 (s)
PROSTATEx Challenge	2016	✓	✓	✓	✓	5-Gleason Grade Group	538 (i)
PROSTATEx-2 Challenge	2017	✓	✓	✓	✓	5-Gleason Grade Group	162 (i)
QIN-PROSTATE Repeatability	2018	✓			✓	WG, PZ, TZ	15 (s)

given noise z, E_z is the expected value over all random inputs to the generator. In effect, the expected value over all generated fake instances $G_g(z)$ and $D_d(x)$ is the discriminator's estimate of the probability that a fake instance is real.

B. EVALUATION TECHNIQUES

The segmentation performance of algorithm are evaluated by comparing the segmented image, P to the reference manually segmented image, T. Evaluation metrics are calculated by per slice comparison and then taking the average for every patient. Different quantitative metrics for evaluating model performance are described in the following subsections.

1) DICE SIMILARITY COEFFICIENT (DSC)

The segmentation performance of prostate MRI is evaluated based on intersection between *manually segmented image* and *predicted segmented image* sets using Dice similarity coefficient (DSC) [206]. In essence, DSC measures the resemblance of elements between *predicted segmented image* and *manually segmented image* sets given as

$$DSC = 2\frac{|T \bigcap P|}{|T| + |P|} \times 100, \tag{13}$$

where $|T|$ and $|P|$ represent the number of elements in manually segmented image and predicted segmented image sets, respectively. The DSC values range between 0 to 1, with 1 indicating the best-case scenario.

2) SENSITIVITY (SEN)

In a two-class scenario, sensitivity measures the correct detection ratio of true positives, given as

$$SEN = \frac{|TP|}{|TP| + |FN|} \times 100, \tag{14}$$

where TP is the number of "true positive," that positive pixels correctly identified, FP is the number of "false positive" that negative pixels incorrectly identified, and FN is the number of "false negative" that positive pixels that have been incorrectly identified.

3) SPECIFICITY (SP)

Specificity measures the correct detection ratio of true negatives,

$$SP = \frac{|TN|}{|TN| + |FP|} \times 100. \tag{15}$$

4) RELATIVE VOLUME DIFFERENCE (RVD)

Relative volume difference [216] is computed as follow:

$$RVD = (\frac{|T|}{|P|} - 1) \times 100, \tag{16}$$

where $|T|$ and $|P|$ represent the number of elements in reference mask and predicted mask image sets, respectively

5) 95% HAUSDORFF DISTANCE (HD)

95% Hausdorff distance measure 95th percentile of the maximum distance of reference image set to nearest point in predicted image set [217]. 95% Hausdorff distance can be computed as follow:

$$HD(P, T) = max[d(T, P), d(P, T)], \tag{17}$$

where T and P are finite set.

6) AVERAGE SURFACE DISTANCE (ASD)

Average surface distance [218] can be computed as follows:

$$ASD = \frac{1}{|T| + |P|}[d(T, P), d(P, T)] \tag{18}$$

7) AVERAGE ABSOLUTE DISTANCE (AAD)

Average absolute distance measures the distance from reference mask boundary to the predicted mask boundary. AAD can be computed as follows:

$$AAD = \frac{1}{|T|}[d(T, P)] \tag{19}$$

8) MAXIMUM ABSOLUTE DISTANCE (MAD)

Maximum absolute distance can be computed as follows:

$$MAD = max[d(T, P)] \tag{20}$$

IX. PUBLICLY AVAILABLE PROSTATE MRI DATASETS

The publicly available prostate MRI dataset are presented in Table 9, detailing the MRI modality, ground truth label and number of images or subjects. There are mainly 3 groups of

dataset depending on ground truth label; solely on segmentation, solely on CaP classification or staging and combined segmentation and classification. The PROMISE12 [206], NCI-ISBI 2013 and QIN-PROSTATE Repeatability are only for segmentation but the I2CVB [33] can be used for development of zonal segmentation and cancer detection methods. On the other hand, both PROSTATEx and PROSTATEx-2 are used for development of diagnostic classification of clinically significant prostate lesions, whereas the ground truth is labelled using 5-class of Gleason Grade Group which was graded by an experienced pathologist [202]. Basically, the PROSTATEx is a subset of PROSTATEx-2. Both challenges aim to promote the advancement of image based computational techniques and thereby reducing unnecessary biopsies. The dataset summarized in Table 9 can be found in their corresponding websites as listed below.

1) https://PROMISE-12.grand-challenge.org/.
2) https://wiki.cancerimagingarchive.net/display/DOI/NCI-ISBI+2013+Challenge%3A+Automated + Segmentation+of+ Prostate+Structures.
3) https://i2cvb.github.io/.
4) https://wiki.cancerimagingarchive.net/display/Public/SPIE-AAPM-NCI+PROSTATEx+Challenges.
5) https://www.aapm.org/GrandChallenge/PROSTATEx-2/default.asp.
6) https://wiki.cancerimagingarchive.net/display/Public/QIN-PROSTATE-Repeatability.

A new accessible dataset of prostate 3T MRI collection consisting of 11 patients with 229 T2-weighted MR slices collected from Universiti Kebangsaan Malaysia Medical Center (UKMMC) is available at http://bit.ly/prostatehukm. The images were acquired using a 3-Tesla Siemens TIM MRI scanner with surface coil. The image dimensions are 384 × 384 and 320×320, with thickness of 3 mm. The dataset image masks are labeled for 2 classes, whole prostate gland (WG), and background. The dataset was used in the evaluation of patch-wise FCN, SegNet, U-Net and DeepLabV3+ [173].

A. DISCUSSION

In this review, we explored the techniques of machine learning and new, deep-learning segmentation methods of different modalities prostate MRI. The latest state-of-the-art segmentation approaches are mainly based on CNN for the segmentation of prostate MRI and can be categorized into four groups: feature encoder based techniques, upsampling based techniques, increased resolution based techniques and region-based proposal. The detail of the literature work of machine learning and deep learning methods is given in Table 1, 2, 3, 4, 5, 6 and 7. In addition, the use of the generative adversarial network with CNN for segmentation of prostate MRI is given in Table 7.

In light of the review on 8-group of segmentation techniques; atlas, deformable model, feature encoder, upsampling, resolution increment of features, and regional proposal, we can draw the following summary of trend on the segmentation work.

Clearly the atlas and deformable based segmentation remained popular from 2005 only until 2017. This is mainly due to the major breakthrough of deep learning technique, which started to gain interest after the introduction of ImageNet dataset in 2009. The earliest deep learning prostate segmentation method was in 2013, which was based on a feature encoder framework In fact, hybrid of feature encoder with deformable [103] and atlas [105] was proposed in 2015 and 2017, respectively. However, beyond 2017, there was no new hybrid of deep learning + atlas/deformable model being proposed. Notably, over the period of 2013 to 2020, a total of 7 segmentation methods based on feature encoder was proposed which means at the rate of 1 paper/year.

The upsampling method started to be used for prostate MRI segmentation in 2016 and until 2020, there were 25 papers proposed for prostate segmentation which is equivalent to 6.25 papers/year. The regional proposal method only has 4 proposed methods from 2018 to 2020 which is at the rate of 2 papers/year. Prostate segmentation methods based on GAN also have a low number of papers, with 9 papers published from 2017 to 2020, equivalent to 3 papers/year. On the other hand, the resolution method is considered as the most popular among the 5 deep learning methods since there were 28 papers published on the method in just over 1 year, from 2019 to 2020.

In the medical image dataset confronting an issue of class differences, to resolve this issue, the different loss function is explained in this survey, as shown in Figure 6.

The challenging task with prostate MRI is the delineation of the prostate that varies from patient to patient and having an impact in different modalities. Making a fair distinction between quantitative analysis of the various studies is not easy. This fact is interpreted by different factors which play its part.

Large dataset with precise annotation by the radiologist and pathologist are still lacking. Different datasets are utilized for the assessment of the developed algorithm and faces a lack of standardization regarding experimental evaluation. The similar view concluded by [219] supporting the above argument, that experimental results are not validated using common datasets which results in the inability to compare the various studies.

The literature work shows that deep convolutional neural networks have performed better than machine learning techniques. Several deep learning methods have been trained and tested on personal data and publicly available datasets, which provide a better platform for transparent evaluation and comparison of DCNN and also to exploit the capabilities of DCNN in segmentation of prostate MRI.

Enhanced feature-based techniques are computationally less expensive, and have fewer parameters than the feature encoder based techniques, upsampling based techniques and increased resolution based techniques.

The main problem in research on prostate cancer diagnosis is the availability of a large dataset with precise annotation by the radiologist and pathologist. Especially, the process of annotation of prostate MRI needs sufficient effort to find the pathology in the MRI images.

X. FUTURE CHALLENGES, PERSPECTIVE AND CONCLUSION

Based on this survey, it is apparent that the ability of DCNN to learn the appropriate features of input images has given them an edge over traditional methods of prostate MRI segmentation. The benefit is pre-processing steps: data augmentation, generative adversarial network, and patch extraction provide sufficient data to enhance the performance of DCNN networks. Moreover the availability of public prostate datasets and the development of advanced deep neural networks as well as powerful hardware for computing play vital roles in better prostate segmentation.

This review article has presented an overview of the segmentation work of prostate MRI covering the traditional method of atlas and deformable model as well and DCNN methods. The background provides information regarding the anatomy, carcinoma and prostate screening and MRI imaging techniques. The methods used for preprocessing of MRI dataset and prostate segmentation are explained in detail in the literature. Moreover, current challenges and possible future research directions have given insight challenges and future perspective. Finally, this survey provide sufficient understanding about the DCNN techniques that have performed very well in prostate MRI segmentation, and also provide information regarding the current and future challenges.

REFERENCES

[1] R. Siegel, D. Naishadham, and A. Jemal, "Cancer statistics, 2013," *CA, Cancer J. Clinicians*, vol. 63, no. 1, pp. 11–30, Jan. 2013.

[2] Cancer Facts and Figures. (2017). *Atlanta: American Cancer Society*. [Online]. Available: https://www.cancer.org/research/cancer-facts-statistics/all-cancer-facts-figures.html

[3] J. C. Weinreb, J. O. Barentsz, P. L. Choyke, F. Cornud, M. A. Haider, K. J. Macura, D. Margolis, M. D. Schnall, F. Shtern, C. M. Tempany, H. C. Thoeny, and S. Verma, "PI-RADS prostate imaging–reporting and data system: 2015, version 2," *Eur. Urol.*, vol. 69, no. 1, pp. 16–40, 2016.

[4] R. L. Siegel, K. D. Miller, and A. Jemal, "Cancer statistics, 2019," *CA, Cancer J. Clinicians*, vol. 69, no. 1, pp. 7–34, 2019.

[5] R. A. Smith, K. S. Andrews, D. Brooks, S. A. Fedewa, D. Manassaram-Baptiste, D. Saslow, O. W. Brawley, and R. C. Wender, "Cancer screening in the united states, 2017: A review of current American cancer society guidelines and current issues in cancer screening," *CA, Cancer J. Clinicians*, vol. 67, no. 2, pp. 100–121, Mar. 2017.

[6] G. L. Lu-Yao, "Outcomes of localized prostate cancer following conservative management," *Jama*, vol. 302, no. 11, pp. 1202–1209, 2009.

[7] J. E. McNeal, E. A. Redwine, F. S. Freiha, and T. A. Stamey, "Zonal distribution of prostatic adenocarcinoma: Correlation with histologic pattern and direction of spread," *Amer. J. Surgical Pathol.*, vol. 12, no. 12, pp. 897–906, 1988.

[8] *The National Cancer Institute (NCI): Prostate Cancer Treatment Stages Prostate Cancer*. Accessed: Jun. 14, 2021. [Online]. Available: http://www.cancer.gov/types/prostate/patient/prostate-treatmentpdq#section/_120

[9] R. M. Martin, L. Vatten, D. Gunnell, and P. Romundstad, "Blood pressure and risk of prostate cancer: Cohort norway (CONOR)," *Cancer Causes Control*, vol. 21, no. 3, pp. 463–472, Mar. 2010.

[10] V. Venkateswaran and L. H. Klotz, "Diet and prostate cancer: Mechanisms of action and implications for chemoprevention," *Nature Rev. Urol.*, vol. 7, no. 8, p. 442, 2010.

[11] D. D. Alexander, P. J. Mink, C. A. Cushing, and B. Sceurman, "A review and meta-analysis of prospective studies of red and processed meat intake and prostate cancer," *Nutrition J.*, vol. 9, no. 1, p. 50, Dec. 2010.

[12] T. Tarver, "Cancer facts & figures 2012. American Cancer Society (ACS)," *J. Consum. Health Internet*, vol. 16, pp. 366–367, Aug. 2012.

[13] E. Giovannucci, Y. Liu, E. A. Platz, M. J. Stampfer, and W. C. Willett, "Risk factors for prostate cancer incidence and progression in the health professionals follow-up study," *Int. J. Cancer*, vol. 121, no. 7, pp. 1571–1578, 2007.

[14] C. Rodriguez, S. J. Freedland, A. Deka, E. J. Jacobs, M. L. McCullough, A. V. Patel, M. J. Thun, and E. E. Calle, "Body mass index, weight change, and risk of prostate cancer in the cancer prevention study II nutrition cohort," *Cancer Epidemiol. Biomarkers Prevention*, vol. 16, no. 1, pp. 63–69, Jan. 2007.

[15] G. D. Steinberg, B. S. Carter, T. H. Beaty, B. Childs, and P. C. Walsh, "Family history and the risk of prostate cancer," *Prostate*, vol. 17, no. 4, pp. 337–347, 1990.

[16] J. He, X. Li, N. Liu, and S. Zhan, "Conditional generative adversarial networks with multi-scale discriminators for prostate MRI segmentation," *Neural Process. Lett.*, vol. 52, no. 2, pp. 1251–1261, 2020.

[17] K.-H. Leissner and L.-E. Tisell, "The weight of the human prostate," *Scandin. J. Urol. Nephrol.*, vol. 13, no. 2, pp. 137–142, Jan. 1979.

[18] S.-J. Zhang, H.-N. Qian, Y. Zhao, K. Sun, H.-Q. Wang, G.-Q. Liang, F.-H. Li, and Z. Li, "Relationship between age and prostate size," *Asian J. Androl.*, vol. 15, no. 1, p. 116, 2013.

[19] D. Bonekamp, M. A. Jacobs, R. El-Khouli, D. Stoianovici, and K. J. Macura, "Advancements in MR imaging of the prostate: From diagnosis to interventions," *RadioGraphics*, vol. 31, no. 3, pp. 677–703, May 2011.

[20] O. S. Lowsley, "The development of the human prostate gland with reference to the development of other structures at the neck of the urinary bladder," *Amer. J. Anatomy*, vol. 13, no. 3, pp. 299–349, 1912.

[21] J. E. McNeal, "The zonal anatomy of the prostate," *Prostate*, vol. 2, no. 1, pp. 35–49, 1981.

[22] D. Cheng and C. M. C. Tempany, "MR imaging of the prostate and bladder," *Seminars Ultrasound, CT MRI*, vol. 19, no. 1, pp. 67–89, Feb. 1998.

[23] K. Y. Kyle and H. Hricak, "Imaging prostate cancer," *Radiologic Clinics North Amer.*, vol. 38, no. 1, pp. 59–85, 2000.

[24] *Surveillance, Epidemiology, and End Results Program. Cancer Stat Facts: Prostate Cancer*, NCI, Bethesda, MD, USA, Jul. 2019.

[25] G. Draisma, R. Etzioni, A. Tsodikov, A. Mariotto, E. Wever, R. Gulati, E. Feuer, and H. de Koning, "Lead time and overdiagnosis in prostate-specific antigen screening: Importance of methods and context," *JNCI J. Nat. Cancer Inst.*, vol. 101, no. 6, pp. 374–383, Mar. 2009.

[26] J. White, B. V. Shenoy, R. F. Tutrone, L. I. Karsh, D. R. Saltzstein, W. J. Harmon, D. L. Broyles, T. E. Roddy, L. R. Lofaro, C. J. Paoli, D. Denham, and M. A. Reynolds, "Clinical utility of the prostate health index (phi) for biopsy decision management in a large group urology practice setting," *Prostate Cancer Prostatic Diseases*, vol. 21, no. 1, pp. 78–84, Apr. 2018.

[27] J. J. Tosoian, S. C. Druskin, D. Andreas, P. Mullane, M. Chappidi, S. Joo, K. Ghabili, J. Agostino, K. J. Macura, H. B. Carter, E. M. Schaeffer, A. W. Partin, L. J. Sokoll, and A. E. Ross, "Use of the prostate health index for detection of prostate cancer: Results from a large academic practice," *Prostate Cancer Prostatic Diseases*, vol. 20, no. 2, pp. 228–233, Jun. 2017.

[28] S. Loeb, M. G. Sanda, D. L. Broyles, S. S. Shin, C. H. Bangma, J. T. Wei, A. W. Partin, G. G. Klee, K. M. Slawin, L. S. Marks, R. H. N. van Schaik, D. W. Chan, L. J. Sokoll, A. B. Cruz, I. A. Mizrahi, and W. J. Catalona, "The prostate health index selectively identifies clinically significant prostate cancer," *J. Urol.*, vol. 193, no. 4, pp. 1163–1169, Apr. 2015.

[29] D. Beyersdorff, A. Winkel, B. Hamm, S. Lenk, S. A. Loening, and M. Taupitz, "MR imaging–guided prostate biopsy with a closed MR unit at 1.5 T: Initial results," *Radiology*, vol. 234, no. 2, pp. 576–581, Feb. 2005.

[30] B. Turkbey, P. A. Pinto, and P. L. Choyke, "Imaging techniques for prostate cancer: Implications for focal therapy," *Nature Rev. Urol.*, vol. 6, no. 4, p. 191, 2009.

[31] B. Turkbey and P. L. Choyke, "Multiparametric MRI and prostate cancer diagnosis and risk stratification," *Current Opinion Urol.*, vol. 22, no. 4, p. 310, 2012.

[32] A. Rampun, L. Zheng, P. Malcolm, B. Tiddeman, and R. Zwiggelaar, "Computer-aided detection of prostate cancer in T2-weighted MRI within the peripheral zone," *Phys. Med. Biol.*, vol. 61, no. 13, p. 4796, 2016.
[33] G. Lemaître, R. Martí, J. Freixenet, J. C. Vilanova, P. M. Walker, and F. Meriaudeau, "Computer-aided detection and diagnosis for prostate cancer based on mono and multi-parametric MRI: A review," *Comput. Biol. Med.*, vol. 60, pp. 8–31, May 2015.
[34] D. Lv, X. Guo, X. Wang, J. Zhang, and J. Fang, "Computerized characterization of prostate cancer by fractal analysis in MR images," *J. Magn. Reson. Imag.*, vol. 30, no. 1, pp. 161–168, Jul. 2009.
[35] S. E. Viswanath, N. B. Bloch, J. C. Chappelow, R. Toth, N. M. Rofsky, E. M. Genega, R. E. Lenkinski, and A. Madabhushi, "Central gland and peripheral zone prostate tumors have significantly different quantitative imaging signatures on 3 tesla endorectal, *in vivo* T2-weighted MR imagery," *J. Magn. Reson. Imag.*, vol. 36, no. 1, pp. 213–224, Jul. 2012.
[36] G. Lemaitre, "Computer-aided diagnosis for prostate cancer using multiparametric magnetic resonance imaging," Ph.D. dissertation, Dept. Softw. Eng., Univ. Burgundy, Dijon, France, 2016.
[37] J. O. Barentsz, J. Richenberg, R. Clements, P. Choyke, S. Verma, G. Villeirs, O. Rouviere, V. Logager, and J. J. Fütterer, "ESUR prostate MR guidelines 2012," *Eur. Radiol.*, vol. 22, no. 4, pp. 746–757, Apr. 2012.
[38] B. Turkbey, O. Aras, N. Karabulut, A. T. Turgut, E. Akpinar, S. Alibek, Y. Pang, S. M. Erturk, R. H. E. Khouli, D. A. Bluemke, and P. L. Choyke, "Diffusion weighted MRI for detecting and monitoring cancer: A review of current applications in body imaging," *Diagnostic Interventional Radiol.*, vol. 18, no. 1, p. 46, 2011.
[39] W. T. Dixon, "Separation of diffusion and perfusion in intravoxel incoherent motion MR imaging: A modest proposal with tremendous potential," *Radiology*, vol. 168, no. 2, pp. 566–567, Aug. 1988.
[40] C. M. A. Hoeks, J. O. Barentsz, T. Hambrock, D. Yakar, D. M. Somford, S. W. T. P. J. Heijmink, T. W. J. Scheenen, P. C. Vos, H. Huisman, I. M. van Oort, J. A. Witjes, A. Heerschap, and J. J. Fütterer, "Prostate cancer: Multiparametric MR imaging for detection, localization, and staging," *Radiology*, vol. 261, no. 1, pp. 46–66, Oct. 2011.
[41] D. M. Somford, J. J. Fütterer, T. Hambrock, and J. O. Barentsz, "Diffusion and perfusion MR imaging of the prostate," *Magn. Reson. Imag. Clinics North Amer.*, vol. 16, no. 4, pp. 685–695, 2008.
[42] J. Hugosson, S. Carlsson, G. Aus, S. Bergdahl, A. Khatami, P. Lodding, C.-G. Pihl, J. Stranne, E. Holmberg, and H. Lilja, "Mortality results from the göteborg randomised population-based prostate-cancer screening trial," *Lancet Oncol.*, vol. 11, no. 8, pp. 725–732, 2010.
[43] T. E. Behrens and H. Johansen-Berg, *Diffusion MRI: From Quantitative Measurement to in-Vivo Neuroanatomy*. New York, NY, USA: Academic Press, 2009.
[44] T. A. G. M. Huisman, "Diffusion-weighted imaging: Basic concepts and application in cerebral stroke and head trauma," *Eur. Radiol.*, vol. 13, no. 10, pp. 2283–2297, Oct. 2003.
[45] J. Mohan, V. Krishnaveni, and Y. Guo, "A survey on the magnetic resonance image denoising methods," *Biomed. Signal Process. Control*, vol. 9, pp. 56–69, Jan. 2014.
[46] H. Gudbjartsson and S. Patz, "The Rician distribution of noisy MRI data," *Magn. Reson. Med.*, vol. 34, no. 6, pp. 910–914, Dec. 1995.
[47] J. Manjon, J. Carbonellcaballero, J. Lull, G. Garciamarti, L. Martibonmati, and M. Robles, "MRI denoising using non-local means," *Med. Image Anal.*, vol. 12, no. 4, pp. 514–523, Aug. 2008.
[48] S. Ozer, M. A. Haider, D. L. Langer, T. H. Van der Kwast, A. J. Evans, M. N. Wernick, J. Trachtenberg, and I. S. Yetik, "Prostate cancer localization with multispectral MRI based on relevance vector machines," in *Proc. IEEE Int. Symp. Biomed. Imag., From Nano Macro*, Jun. 2009, pp. 73–76.
[49] J. Joseph and R. Periyasamy, "An image driven bilateral filter with adaptive range and spatial parameters for denoising magnetic resonance images," *Comput. Electr. Eng.*, vol. 69, pp. 782–795, Jul. 2018.
[50] D. Ampeliotis, A. Antonakoudi, K. Berberidis, and E. Z. Psarakis, "Computer aided detection of prostate cancer using fused information from dynamic contrast enhanced and morphological magnetic resonance images," in *Proc. IEEE Int. Conf. Signal Process. Commun.*, Nov. 2007, pp. 888–891.
[51] D. Ampeliotis, A. Antonakoudi, K. Berberidis, E. Z. Psarakis, and A. Kounoudes, "A computer-aided system for the detection of prostate cancer based on magnetic resonance image analysis," in *Proc. 3rd Int. Symp. Commun., Control Signal Process.*, Mar. 2008, pp. 1372–1377.
[52] S. Mallat, *A Wavelet Tour of Signal Processing: The Sparse Way*, 3rd ed. London, U.K.: AP Professional, 2009.
[53] S. Saladi and N. A. Prabha, "Analysis of denoising filters on MRI brain images," *Int. J. Imag. Syst. Technol.*, vol. 27, no. 3, pp. 201–208, Sep. 2017.
[54] E. M. Eksioglu and A. K. Tanc, "Denoising AMP for MRI reconstruction: BM3D-AMP-MRI," *SIAM J. Imag. Sci.*, vol. 11, no. 3, pp. 2090–2109, Jan. 2018.
[55] J. C. Reinhold, B. E. Dewey, A. Carass, and J. L. Prince, "Evaluating the impact of intensity normalization on MR image synthesis," *Proc. SPIE*, vol. 10949, Mar. 2019, Art. no. 109493H.
[56] R. C. Gonzalez, R. E. Woods, and S. L. Eddins, *Digital Image Processing Using MATLAB*. London, U.K.: Pearson, 2004.
[57] C. Szegedy, W. Liu, Y. Jia, P. Sermanet, S. Reed, D. Anguelov, D. Erhan, V. Vanhoucke, and A. Rabinovich, "Going deeper with convolutions," in *Proc. IEEE Conf. Comput. Vis. Pattern Recognit. (CVPR)*, Jun. 2015, pp. 1–9.
[58] L. Perez and J. Wang, "The effectiveness of data augmentation in image classification using deep learning," 2017, *arXiv:1712.04621*. [Online]. Available: http://arxiv.org/abs/1712.04621
[59] I. Bankman, *Handbook of Medical Image Processing and Analysis*. Amsterdam, The Netherlands: Elsevier, 2008.
[60] A. Krizhevsky, I. Sutskever, and G. E. Hinton, "ImageNet classification with deep convolutional neural networks," in *Proc. Adv. Neural Inf. Process. Syst.*, 2012, pp. 1097–1105.
[61] K. Simonyan and A. Zisserman, "Very deep convolutional networks for large-scale image recognition," 2014, *arXiv:1409.1556*. [Online]. Available: http://arxiv.org/abs/1409.1556
[62] K. He, X. Zhang, S. Ren, and J. Sun, "Deep residual learning for image recognition," in *Proc. IEEE Conf. Comput. Vis. Pattern Recognit.*, Jun. 2016, pp. 770–778.
[63] F. Chollet, "Xception: Deep learning with depthwise separable convolutions," in *Proc. IEEE Conf. Comput. Vis. Pattern Recognit. (CVPR)*, Jul. 2017, pp. 1251–1258.
[64] Y. Lecun, L. Bottou, Y. Bengio, and P. Haffner, "Gradient-based learning applied to document recognition," *Proc. IEEE*, vol. 86, no. 11, pp. 2278–2324, Nov. 1998.
[65] H. Noh, S. Hong, and B. Han, "Learning deconvolution network for semantic segmentation," in *Proc. IEEE Int. Conf. Comput. Vis. (ICCV)*, Dec. 2015, pp. 1520–1528.
[66] J. Long, E. Shelhamer, and T. Darrell, "Fully convolutional networks for semantic segmentation," in *Proc. IEEE Conf. Comput. Vis. Pattern Recognit.*, Jun. 2015, pp. 3431–3440.
[67] O. Ronneberger, P. Fischer, and T. Brox, "U-Net: Convolutional networks for biomedical image segmentation," in *Proc. Int. Conf. Med. Image Comput. Comput.-Assist. Intervent.* Cham, Switzerland: Springer, 2015, pp. 234–241.
[68] V. Badrinarayanan, A. Kendall, and R. Cipolla, "SegNet: A deep convolutional encoder-decoder architecture for image segmentation," *IEEE Trans. Pattern Anal. Mach. Intell.*, vol. 39, no. 12, pp. 2481–2495, Dec. 2017.
[69] M. Ranzato, F. J. Huang, Y.-L. Boureau, and Y. LeCun, "Unsupervised learning of invariant feature hierarchies with applications to object recognition," in *Proc. IEEE Conf. Comput. Vis. Pattern Recognit.*, Jun. 2007, pp. 1–8.
[70] L.-C. Chen, G. Papandreou, I. Kokkinos, K. Murphy, and A. L. Yuille, "Semantic image segmentation with deep convolutional nets and fully connected CRFs," 2014, *arXiv:1412.7062*. [Online]. Available: http://arxiv.org/abs/1412.7062
[71] L.-C. Chen, G. Papandreou, F. Schroff, and H. Adam, "Rethinking atrous convolution for semantic image segmentation," 2017, *arXiv:1706.05587*. [Online]. Available: http://arxiv.org/abs/1706.05587
[72] J. M. Alvarez, Y. LeCun, T. Gevers, and A. M. Lopez, "Semantic road segmentation via multi-scale ensembles of learned features," in *Proc. Eur. Conf. Comput. Vis.* Berlin, Germany: Springer, 2012, pp. 586–595.
[73] L.-C. Chen, Y. Zhu, G. Papandreou, F. Schroff, and H. Adam, "Encoder-decoder with atrous separable convolution for semantic image segmentation," in *Proc. Eur. Conf. Comput. Vis. (ECCV)*, 2018, pp. 801–818.
[74] R. Girshick, J. Donahue, T. Darrell, and J. Malik, "Rich feature hierarchies for accurate object detection and semantic segmentation," in *Proc. IEEE Conf. Comput. Vis. Pattern Recognit.*, Jun. 2014, pp. 580–587.
[75] J. R. R. Uijlings, K. E. A. van de Sande, T. Gevers, and A. W. M. Smeulders, "Selective search for object recognition," *Int. J. Comput. Vis.*, vol. 104, no. 2, pp. 154–171, Sep. 2013.
[76] R. Girshick, "Fast R-CNN," in *Proc. IEEE Int. Conf. Comput. Vis. (ICCV)*, Santiago, Chile, 2015, pp. 1440–1448.
[77] S. Ren, K. He, R. Girshick, and J. Sun, "Faster R-CNN: Towards real-time object detection with region proposal networks," in *Proc. Adv. Neural Inf. Process. Syst.*, 2015, pp. 91–99.

[78] K. He, G. Gkioxari, P. Dollár, and R. Girshick, "Mask R-CNN," in *Proc. IEEE Int. Conf. Comput. Vis.*, Oct. 2017, pp. 2961–2969.

[79] S. Klein, U. A. van der Heide, I. M. Lips, M. van Vulpen, M. Staring, and J. P. W. Pluim, "Automatic segmentation of the prostate in 3D MR images by atlas matching using localized mutual information," *Med. Phys.*, vol. 35, no. 4, pp. 1407–1417, Mar. 2008.

[80] S. Martin, J. Troccaz, and V. Daanen, "Automated segmentation of the prostate in 3D MR images using a probabilistic atlas and a spatially constrained deformable model," *Med. Phys.*, vol. 37, no. 4, pp. 1579–1590, Mar. 2010.

[81] T. R. Langerak, U. A. van der Heide, A. N. T. J. Kotte, M. A. Viergever, M. van Vulpen, and J. P. W. Pluim, "Label fusion in atlas-based segmentation using a selective and iterative method for performance level estimation (SIMPLE)," *IEEE Trans. Med. Imag.*, vol. 29, no. 12, pp. 2000–2008, Dec. 2010.

[82] J. A. Dowling, J. Fripp, S. Chandra, J. P. W. Pluim, J. Lambert, J. Parker, J. Denham, P. B. Greer, and O. Salvado, "Fast automatic multi-atlas segmentation of the prostate from 3D MR images," in *Proc. Int. Workshop Prostate Cancer Imag.* Berlin, Germany: Springer, 2011, pp. 10–21.

[83] G. Litjens, O. Debats, W. van de Ven, N. Karssemeijer, and H. Huisman, "A pattern recognition approach to zonal segmentation of the prostate on MRI," in *Proc. Int. Conf. Med. Image Comput. Comput.-Assist. Intervent.* Berlin, Germany: Springer, 2012, pp. 413–420.

[84] W. Qiu, J. Yuan, E. Ukwatta, Y. Sun, M. Rajchl, and A. Fenster, "Dual optimization based prostate zonal segmentation in 3D MR images," *Med. Image Anal.*, vol. 18, no. 4, pp. 660–673, May 2014.

[85] V. Giannini, S. Mazzetti, A. Vignati, F. Russo, E. Bollito, F. Porpiglia, M. Stasi, and D. Regge, "A fully automatic computer aided diagnosis system for peripheral zone prostate cancer detection using multi-parametric magnetic resonance imaging," *Computerized Med. Imag. Graph.*, vol. 46, pp. 219–226, Dec. 2015.

[86] J. Zhang, S. Baig, A. Wong, M. A. Haider, and F. Khalvati, "A local ROI-specific atlas-based segmentation of prostate gland and transitional zone in diffusion MRI," *J. Comput. Vis. Imag. Syst.*, vol. 2, no. 1, pp. 1–3, Oct. 2016.

[87] O. Chilali, P. Puech, S. Lakroum, M. Diaf, S. Mordon, and N. Betrouni, "Gland and zonal segmentation of prostate on T2W MR images," *J. Digit. Imag.*, vol. 29, no. 6, pp. 730–736, Dec. 2016.

[88] X. Yang, A. B. Jani, P. J. Rossi, H. Mao, W. J. Curran, and T. Liu, "Patch-based label fusion for automatic multi-atlas-based prostate segmentation in MR images," *Proc. SPIE*, vol. 9786, Mar. 2016, Art. no. 978621.

[89] S. K. Warfield, K. H. Zou, and W. M. Wells, "Simultaneous truth and performance level estimation (STAPLE): An algorithm for the validation of image segmentation," *IEEE Trans. Med. Imag.*, vol. 23, no. 7, pp. 903–921, Jul. 2004.

[90] Y. Zhu, S. Williams, and R. Zwiggelaar, "A hybrid ASM approach for sparse volumetric data segmentation," *Pattern Recognit. Image Anal. Adv. Math. Theory Appl.*, vol. 15, no. 2, pp. 346–349, 2005.

[91] S. Vikal, S. Haker, C. Tempany, and G. Fichtinger, "Prostate contouring in MRI-guided biopsy," *Proc. SPIE*, vol. 7259, Mar. 2009, Art. no. 72594A.

[92] Y. Gao, R. Sandhu, G. Fichtinger, and A. R. Tannenbaum, "A coupled global registration and segmentation framework with application to magnetic resonance prostate imagery," *IEEE Trans. Med. Imag.*, vol. 29, no. 10, pp. 1781–1794, Oct. 2010.

[93] N. Makni, P. Puech, R. Lopes, A.-S. Dewalle, O. Colot, and N. Betrouni, "Combining a deformable model and a probabilistic framework for an automatic 3D segmentation of prostate on MRI," *Int. J. Comput. Assist. Radiol. surgery*, vol. 4, no. 2, p. 181, 2009.

[94] T. F. Cootes and C. J. Taylor, "Statistical models of appearance for medical image analysis and computer vision," *Proc. SPIE*, vol. 4322, pp. 236–248, Jul. 2001.

[95] S. S. Chandra, J. A. Dowling, K.-K. Shen, P. Raniga, J. P. W. Pluim, P. B. Greer, O. Salvado, and J. Fripp, "Patient specific prostate segmentation in 3-D magnetic resonance images," *IEEE Trans. Med. Imag.*, vol. 31, no. 10, pp. 1955–1964, Oct. 2012.

[96] R. Toth and A. Madabhushi, "Multifeature landmark-free active appearance models: Application to prostate MRI segmentation," *IEEE Trans. Med. Imag.*, vol. 31, no. 8, pp. 1638–1650, Aug. 2012.

[97] Y. Yin, S. V. Fotin, S. Periaswamy, J. Kunz, H. Haldankar, N. Muradyan, F. Cornud, B. Turkbey, and P. Choyke, "Fully automated prostate segmentation in 3D MR based on normalized gradient fields cross-correlation initialization and logismos refinement," *Proc. SPIE*, vol. 8314, Feb. 2012, Art. no. 831406.

[98] B. Maan and F. van der Heijden, "Prostate MR image segmentation using 3D active appearance models," *MICCAI Grand Challenge, Prostate MR Image Segmentation*, vol. 2012, pp. 1–8, Oct. 2012.

[99] S. Ghose, A. Oliver, R. Marti, X. Lladó, J. Freixenet, J. Mitra, J. C. Vilanova, and F. Meriaudeau, "A hybrid framework of multiple active appearance models and global registration for 3D prostate segmentation in MRI," *Proc. SPIE*, vol. 8314, Feb. 2012, Art. no. 83140S.

[100] F. Khalvati, A. Salmanpour, S. Rahnamayan, M. A. Haider, and H. R. Tizhoosh, "Sequential registration-based segmentation of the prostate gland in MR image volume," *J. Digit. Imag.*, vol. 29, no. 2, pp. 254–263, 2016.

[101] L. Rundo, C. Militello, G. Russo, A. Garufi, S. Vitabile, M. Gilardi, and G. Mauri, "Automated prostate gland segmentation based on an unsupervised fuzzy C-means clustering technique using multispectral T1W and T2W MR imaging," *Information*, vol. 8, no. 2, p. 49, Apr. 2017.

[102] S. Liao, Y. Gao, A. Oto, and D. Shen, "Representation learning: A unified deep learning framework for automatic prostate MR segmentation," in *Proc. Int. Conf. Med. Image Comput. Comput.-Assist. Intervent.* Berlin, Germany: Springer, 2013, pp. 254–261.

[103] Y. Guo, Y. Gao, and D. Shen, "Deformable MR prostate segmentation via deep feature learning and sparse patch matching," *IEEE Trans. Med. Imag.*, vol. 35, no. 4, pp. 1077–1089, Apr. 2016.

[104] R. Cheng, "Active appearance model and deep learning for more accurate prostate segmentation on MRI," *Proc. SPIE*, vol. 9784, Mar. 2016, Art. no. 97842I.

[105] H. Jia, Y. Xia, W. Cai, M. Fulham, and D. D. Feng, "Prostate segmentation in MR images using ensemble deep convolutional neural networks," in *Proc. IEEE 14th Int. Symp. Biomed. Imag. (ISBI)*, Apr. 2017, pp. 762–765.

[106] Y. Ou, A. Sotiras, N. Paragios, and C. Davatzikos, "DRAMMS: Deformable registration via attribute matching and mutual-saliency weighting," *Med. Image Anal.*, vol. 15, no. 4, pp. 622–639, Aug. 2011.

[107] T. Clark, J. Zhang, S. Baig, A. Wong, M. A. Haider, and F. Khalvati, "Fully automated segmentation of prostate whole gland and transition zone in diffusion-weighted MRI using convolutional neural networks," *J. Med. Imag.*, vol. 4, no. 4, 2017, Art. no. 041307.

[108] C. Szegedy, S. Ioffe, V. Vanhoucke, and A. Alemi, "Inception-v4, inception-ResNet and the impact of residual connections on learning," 2016, *arXiv:1602.07261*. [Online]. Available: http://arxiv.org/abs/1602.07261

[109] J. Mun, W.-D. Jang, D. J. Sung, and C.-S. Kim, "Comparison of objective functions in CNN-based prostate magnetic resonance image segmentation," in *Proc. IEEE Int. Conf. Image Process. (ICIP)*, Sep. 2017, pp. 3859–3863.

[110] T. Brosch, J. Peters, A. Groth, T. Stehle, and J. Weese, "Deep learning-based boundary detection for model-based segmentation with application to MR prostate segmentation," in *Proc. Int. Conf. Med. Image Comput. Comput.-Assist. Intervent.* Cham, Switzerland: Springer, 2018, pp. 515–522.

[111] O. Ecabert, J. Peters, H. Schramm, C. Lorenz, J. von Berg, M. J. Walker, M. Vembar, M. E. Olszewski, K. Subramanyan, G. Lavi, and J. Weese, "Automatic model-based segmentation of the heart in CT images," *IEEE Trans. Med. Imag.*, vol. 27, no. 9, pp. 1189–1201, Sep. 2008.

[112] D. Karimi, G. Samei, C. Kesch, G. Nir, and S. E. Salcudean, "Prostate segmentation in MRI using a convolutional neural network architecture and training strategy based on statistical shape models," *Int. J. Comput. Assist. Radiol. Surgery*, vol. 13, no. 8, pp. 1211–1219, Aug. 2018.

[113] Z. Wang, C. Liu, D. Cheng, L. Wang, X. Yang, and K.-T. Cheng, "Automated detection of clinically significant prostate cancer in mp-MRI images based on an end-to-end deep neural network," *IEEE Trans. Med. Imag.*, vol. 37, no. 5, pp. 1127–1139, May 2018.

[114] Q. Liu, M. Fu, X. Gong, and H. Jiang, "Densely dilated spatial pooling convolutional network using benign loss functions for imbalanced volumetric prostate segmentation," 2018, *arXiv:1801.10517*. [Online]. Available: http://arxiv.org/abs/1801.10517

[115] Y. Song, Y.-D. Zhang, X. Yan, H. Liu, M. Zhou, B. Hu, and G. Yang, "Computer-aided diagnosis of prostate cancer using a deep convolutional neural network from multiparametric MRI," *J. Magn. Reson. Imag.*, vol. 48, no. 6, pp. 1570–1577, Dec. 2018.

[116] R. Cheng, "Fully automated prostate whole gland and central gland segmentation on MRI using holistically nested networks with short connections," *J. Med. Imag.*, vol. 6, no. 2, 2019, Art. no. 024007.

[117] Y. Liu, K. Sung, G. Yang, S. A. Mirak, M. Hosseiny, A. Azadikhah, X. Zhong, R. E. Reiter, Y. Lee, and S. S. Raman, "Automatic prostate zonal segmentation using fully convolutional network with feature pyramid attention," *IEEE Access*, vol. 7, pp. 163626–163632, 2019.

[118] H. Li, P. Xiong, J. An, and L. Wang, "Pyramid attention network for semantic segmentation," 2018, *arXiv:1805.10180*. [Online]. Available: http://arxiv.org/abs/1805.10180

[119] I. R. Abdelmaksoud, M. Ghazal, A. Shalaby, M. Elmogy, A. Aboulfotouh, M. A. El-Ghar, R. Keynton, and A. El-Baz, "An accurate system for prostate cancer localization from diffusion-weighted MRI," in *Proc. IEEE Int. Conf. Imag. Syst. Techn. (IST)*, Dec. 2019, pp. 1–5.

[120] K. A. Eppenhof, M. Maspero, M. Savenije, J. de Boer, J. van der Voort Zyp, B. W. Raaymakers, A. Raaijmakers, M. Veta, C. van den Berg, and J. P. Pluim, "Fast contour propagation for MR-guided prostate radiotherapy using convolutional neural networks," *Med. Phys.*, vol. 47, no. 3, pp. 1238–1248, 2020.

[121] M. Arif, I. G. Schoots, J. C. Tovar, C. H. Bangma, G. P. Krestin, M. J. Roobol, W. Niessen, and J. F. Veenland, "Clinically significant prostate cancer detection and segmentation in low-risk patients using a convolutional neural network on multi-parametric MRI," *Eur. Radiol.*, vol. 30, no. 12, pp. 6582–6592, 2020.

[122] D. K. Lee, D. J. Sung, C.-S. Kim, Y. Heo, J. Y. Lee, B. J. Park, and M. J. Kim, "Three-dimensional convolutional neural network for prostate MRI segmentation and comparison of prostate volume measurements by use of artificial neural network and ellipsoid formula," *Amer. J. Roentgenol.*, vol. 214, no. 6, pp. 1229–1238, Jun. 2020.

[123] A. Tewari, R. Indudhara, K. Shinohara, E. Schalow, M. Woods, R. Lee, C. Anderson, and P. Narayan, "Comparison of transrectal ultrasound prostatic volume estimation with magnetic resonance imaging volume estimation and surgical specimen weight in patients with benign prostatic hyperplasia," *J. Clin. Ultrasound*, vol. 24, no. 4, pp. 169–174, May 1996.

[124] X. Yang, C. Liu, Z. Wang, J. Yang, H. L. Min, L. Wang, and K.-T. Cheng, "Co-trained convolutional neural networks for automated detection of prostate cancer in multi-parametric MRI," *Med. Image Anal.*, vol. 42, pp. 212–227, Dec. 2017.

[125] A. Meyer, G. Chlebus, M. Rak, D. Schindele, M. Schostak, B. van Ginneken, A. Schenk, H. Meine, H. K. Hahn, A. Schreiber, and C. Hansen, "Anisotropic 3D multi-stream CNN for accurate prostate segmentation from multi-planar MRI," *Comput. Methods Programs Biomed.*, vol. 200, Mar. 2021, Art. no. 105821.

[126] A. Mehrtash, M. Ghafoorian, G. Pernelle, A. Ziaei, F. G. Heslinga, K. Tuncali, A. Fedorov, R. Kikinis, C. M. Tempany, W. M. Wells, P. Abolmaesumi, and T. Kapur, "Automatic needle segmentation and localization in MRI with 3-D convolutional neural networks: Application to MRI-targeted prostate biopsy," *IEEE Trans. Med. Imag.*, vol. 38, no. 4, pp. 1026–1036, Apr. 2019.

[127] M. N. N. To, D. Q. Vu, B. Turkbey, P. L. Choyke, and J. T. Kwak, "Deep dense multi-path neural network for prostate segmentation in magnetic resonance imaging," *Int. J. Comput. Assist. Radiol. Surgery*, vol. 13, no. 11, pp. 1687–1696, Nov. 2018.

[128] I. Reda, A. El-Baz, M. Ghazal, A. Shalaby, M. Elmogy, A. Aboulfotouh, M. A. El-Ghar, M. El-Melegy, A. Khalil, and R. Keynton, "Detecting and localizing prostate cancer from diffusion-weighted magnetic resonance imaging," in *Proc. IEEE Int. Conf. Image Process. (ICIP)*, Sep. 2019, pp. 1405–1409.

[129] R. Cao, A. M. Bajgiran, S. A. Mirak, S. Shakeri, X. Zhong, D. Enzmann, S. Raman, and K. Sung, "Joint prostate cancer detection and Gleason score prediction in mp-MRI via FocalNet," *IEEE Trans. Med. Imag.*, vol. 38, no. 11, pp. 2496–2506, Nov. 2019.

[130] G. Huang, Z. Liu, L. Van Der Maaten, and K. Q. Weinberger, "Densely connected convolutional networks," in *Proc. IEEE Conf. Comput. Vis. Pattern Recognit. (CVPR)*, Jul. 2017, pp. 4700–4708.

[131] Z. Tian, L. Liu, Z. Zhang, and B. Fei, "PSNet: Prostate segmentation on MRI based on a convolutional neural network," *J. Med. Imag.*, vol. 5, no. 2, 2018, Art. no. 021208.

[132] T. Hassanzadeh, L. G. C. Hamey, and K. Ho-Shon, "Convolutional neural networks for prostate magnetic resonance image segmentation," *IEEE Access*, vol. 7, pp. 36748–36760, 2019.

[133] Y. Yuan, W. Qin, X. Guo, M. Buyyounouski, S. Hancock, B. Han, and L. Xing, "Prostate segmentation with encoder-decoder densely connected convolutional network (Ed-Densenet)," in *Proc. IEEE 16th Int. Symp. Biomed. Imag. (ISBI)*, Apr. 2019, pp. 434–437.

[134] C. Jensen, K. S. Sørensen, C. K. Jørgensen, C. W. Nielsen, P. C. Høy, N. C. Langkilde, and L. R. Østergaard, "Prostate zonal segmentation in 1.5T and 3T T2W MRI using a convolutional neural network," *J. Med. Imag.*, vol. 6, no. 1, 2019, Art. no. 014501.

[135] Q. Zhu, B. Du, B. Turkbey, P. L. Choyke, and P. Yan, "Deeply-supervised CNN for prostate segmentation," in *Proc. Int. Joint Conf. Neural Netw. (IJCNN)*, May 2017, pp. 178–184.

[136] R. Cao, X. Zhong, S. Shakeri, A. M. Bajgiran, S. A. Mirak, D. Enzmann, S. S. Raman, and K. Sung, "Prostate cancer detection and segmentation in multi-parametric MRI via CNN and conditional random field," in *Proc. IEEE 16th Int. Symp. Biomed. Imag. (ISBI)*, Apr. 2019, pp. 1900–1904.

[137] S. Li, Y. Chen, S. Yang, and W. Luo, "Cascade dense-U-Net for prostate segmentation in MR images," in *Proc. Int. Conf. Intell. Comput.* Cham, Switzerland: Springer, 2019, pp. 481–490.

[138] P. Zhong, J. Wu, Z. Yuan, Y. Zhang, and X. Tang, "3D fully convolutional network incorporating Savitzky-Golay filtering for prostate segmentation," in *Proc. 3rd Int. Symp. Image Comput. Digit. Med.*, 2019, pp. 88–91.

[139] X. Huang, B. Liu, J. Hao, H. Nguyen, M. V. Knopp, Q. Miao, and G. Jia, "Automatic segmentation of prostate structures using a convolutional neural network from multiparametric MRI," in *Proc. 3rd Int. Symp. Image Comput. Digit. Med.*, 2019, pp. 92–96.

[140] H. Ocal and N. Barisci, "Prostate segmentation via fusing the nested-V-Net3D and V-Net2D," in *Proc. 1st Int. Informat. Softw. Eng. Conf. (UBMYK)*, Nov. 2019, pp. 1–4.

[141] J. Kang, G. Samarasinghe, U. Senanayake, S. Conjeti, and A. Sowmya, "Deep learning for volumetric segmentation in spatio-temporal data: Application to segmentation of prostate in DCE-MRI," in *Proc. IEEE 16th Int. Symp. Biomed. Imag. (ISBI)*, Apr. 2019, pp. 61–65.

[142] X. Ma, D. Xie, J. Fang, and S. Zhan, "Segmentation of prostate peripheral zone based on multi-scale features enhancement," in *Proc. 3rd Int. Symp. Image Comput. Digit. Med.*, 2019, pp. 349–353.

[143] F. Wang, M. Jiang, C. Qian, S. Yang, C. Li, H. Zhang, X. Wang, and X. Tang, "Residual attention network for image classification," in *Proc. IEEE Conf. Comput. Vis. Pattern Recognit. (CVPR)*, Jul. 2017, pp. 3156–3164.

[144] J. Van, C. Yoon, J. Glavis-Bloom, M. Bardis, A. Ushinsky, D. S. Chow, P. Chang, R. Houshyar, C. Chantaduly, W. A. Grant, and D. Fujimoto, "Deep learning hybrid 3D/2D convolutional neural network for prostate MRI recognition," *J. Clin. Oncol.*, vol. 37, no. 15, May 2019, Art. no. e16600.

[145] Y. Chen, S. Li, S. Yang, and W. Luo, "Scale normalization cascaded dense-U-Net for prostate segmentation in MR images," in *Proc. Int. Conf. Image Graph.* Cham, Switzerland: Springer, 2019, pp. 538–547.

[146] L. Rundo, C. Han, Y. Nagano, J. Zhang, R. Hataya, C. Militello, A. Tangherloni, M. S. Nobile, C. Ferretti, D. Besozzi, M. C. Gilardi, S. Vitabile, G. Mauri, H. Nakayama, and P. Cazzaniga, "USE-Net: Incorporating squeeze-and-excitation blocks into U-Net for prostate zonal segmentation of multi-institutional MRI datasets," *Neurocomputing*, vol. 365, pp. 31–43, Nov. 2019.

[147] I. P. Astono, J. S. Welsh, S. Chalup, and P. Greer, "Optimisation of 2D U-Net model components for automatic prostate segmentation on MRI," *Appl. Sci.*, vol. 10, no. 7, p. 2601, Apr. 2020.

[148] G. L. F. da Silva, P. S. Diniz, J. L. Ferreira, J. V. F. França, A. C. Silva, A. C. de Paiva, and E. A. A. de Cavalcanti, "Superpixel-based deep convolutional neural networks and active contour model for automatic prostate segmentation on 3D MRI scans," *Med. Biol. Eng. Comput.*, vol. 58, no. 9, pp. 1947–1964, Sep. 2020.

[149] M. Baldeon-Calisto and S. K. Lai-Yuen, "AdaResU-Net: Multiobjective adaptive convolutional neural network for medical image segmentation," *Neurocomputing*, vol. 392, pp. 325–340, Jun. 2020.

[150] W. Zhou, X. Tao, Z. Wei, and L. Lin, "Automatic segmentation of 3D prostate MR images with iterative localization refinement," *Digit. Signal Process.*, vol. 98, Mar. 2020, Art. no. 102649.

[151] A. Meyer, A. Mehrtash, M. Rak, D. Schindele, M. Schostak, C. Tempany, T. Kapur, P. Abolmaesumi, A. Fedorov, and C. Hansen, "Automatic high resolution segmentation of the prostate from multi-planar MRI," in *Proc. IEEE 15th Int. Symp. Biomed. Imag. (ISBI)*, Apr. 2018, pp. 177–181.

[152] G. Mooij, I. Bagulho, and H. Huisman, "Automatic segmentation of prostate zones," 2018, *arXiv:1806.07146*. [Online]. Available: http://arxiv.org/abs/1806.07146

[153] F. Milletari, N. Navab, and S.-A. Ahmadi, "V-Net: Fully convolutional neural networks for volumetric medical image segmentation," in *Proc. 4th Int. Conf. 3D Vis. (3DV)*, Oct. 2016, pp. 565–571.

[154] L. Yu, X. Yang, H. Chen, J. Qin, and P. A. Heng, "Volumetric ConvNets with mixed residual connections for automated prostate segmentation from 3D MR images," in *Proc. 31st AAAI Conf. Artif. Intell.*, 2017, pp. 1–7.

[155] P. Lapa, I. Gonçalves, L. Rundo, and M. Castelli, "Semantic learning machine improves the CNN-based detection of prostate cancer in non-contrast-enhanced MRI," in *Proc. Genetic Evol. Comput. Conf. Companion*, Jul. 2019, pp. 1837–1845.

[156] B. Wang, "Automatic MRI prostate segmentation using 3D deeply supervised FCN with concatenated atrous convolution," *Proc. SPIE*, vol. 10950, Mar. 2019, Art. no. 109503X.

[157] Y. Zhu, R. Wei, G. Gao, L. Ding, X. Zhang, X. Wang, and J. Zhang, "Fully automatic segmentation on prostate MR images based on cascaded fully convolution network," *J. Magn. Reson. Imag.*, vol. 49, no. 4, pp. 1149–1156, Apr. 2019.

[158] Z. Khan, N. Yahya, K. Alsaih, and F. Meriaudeau, "Segmentation of prostate in MRI images using depth separable convolution operations," in *Proc. Int. Conf. Intell. Hum. Comput. Interact.* Cham, Switzerland: Springer, 2020, pp. 132–141.

[159] H. Jia, Y. Song, H. Huang, W. Cai, and Y. Xia, "HD-Net: Hybrid discriminative network for prostate segmentation in MR images," in *Proc. Int. Conf. Med. Image Comput. Comput.-Assist. Intervent.* Cham, Switzerland: Springer, 2019, pp. 110–118.

[160] L. Geng, J. Wang, Z. Xiao, J. Tong, F. Zhang, and J. Wu, "Encoder-decoder with dense dilated spatial pyramid pooling for prostate MR images segmentation," *Comput. Assist. Surgery*, vol. 24, no. 2, pp. 13–19, Oct. 2019.

[161] Z. Khan, N. Yahya, K. Alsaih, and F. Meriaudeau, "Zonal segmentation of prostate T2W-MRI using atrous convolutional neural network," in *Proc. IEEE Student Conf. Res. Develop. (SCOReD)*, Oct. 2019, pp. 95–99.

[162] N. Ghavami, Y. Hu, E. Gibson, E. Bonmati, M. Emberton, C. M. Moore, and D. C. Barratt, "Automatic segmentation of prostate MRI using convolutional neural networks: Investigating the impact of network architecture on the accuracy of volume measurement and MRI-ultrasound registration," *Med. Image Anal.*, vol. 58, Dec. 2019, Art. no. 101558.

[163] K. Yan, X. Wang, J. Kim, M. Khadra, M. Fulham, and D. Feng, "A propagation-DNN: Deep combination learning of multi-level features for MR prostate segmentation," *Comput. Methods Programs Biomed.*, vol. 170, pp. 11–21, Mar. 2019.

[164] Y. Zhang, J. Wu, W. Chen, Y. Chen, and X. Tang, "Prostate segmentation using Z-Net," in *Proc. IEEE 16th Int. Symp. Biomed. Imag. (ISBI)*, Apr. 2019, pp. 11–14.

[165] S. Liu, H. Zheng, Y. Feng, and W. Li, "Prostate cancer diagnosis using deep learning with 3D multiparametric MRI," *Proc. SPIE*, vol. 10134, Mar. 2017, Art. no. 1013428.

[166] S. Motamed, I. Gujrathi, D. Deniffel, A. Oentoro, M. A. Haider, and F. Khalvati, "A transfer learning approach for automated segmentation of prostate whole gland and transition zone in diffusion weighted MRI," 2019, *arXiv:1909.09541*. [Online]. Available: http://arxiv.org/abs/1909.09541

[167] R. Alkadi, F. Taher, A. El-baz, and N. Werghi, "A deep learning-based approach for the detection and localization of prostate cancer in T2 magnetic resonance images," *J. Digit. Imag.*, vol. 32, no. 5, pp. 793–807, Oct. 2019.

[168] P. Zaffino, G. Pernelle, A. Mastmeyer, A. Mehrtash, H. Zhang, R. Kikinis, T. Kapur, and M. F. Spadea, "Fully automatic catheter segmentation in MRI with 3D convolutional neural networks: Application to MRI-guided gynecologic brachytherapy," *Phys. Med. Biol.*, vol. 64, no. 16, Aug. 2019, Art. no. 165008.

[169] H. Xu, J. S. H. Baxter, O. Akin, and D. Cantor-Rivera, "Prostate cancer detection using residual networks," *Int. J. Comput. Assist. Radiol. Surgery*, vol. 14, no. 10, pp. 1647–1650, Oct. 2019.

[170] H. Pan, Y. Feng, Q. Chen, C. Meyer, and X. Feng, "Prostate segmentation from 3D MRI using a two-stage model and variable-input based uncertainty measure," in *Proc. IEEE 16th Int. Symp. Biomed. Imag. (ISBI)*, Apr. 2019, pp. 468–471.

[171] Q. Zhu, B. Du, and P. Yan, "Boundary-weighted domain adaptive neural network for prostate MR image segmentation," *IEEE Trans. Med. Imag.*, vol. 39, no. 3, pp. 753–763, Mar. 2020.

[172] X. Si, Z. Tian, X. Li, Z. Chen, G. Li, and J. D. Dormer, "Multi-step segmentation for prostate MR image based on reinforcement learning," *Proc. SPIE*, vol. 11315, Mar. 2020, Art. no. 113152R.

[173] Z. Khan, N. Yahya, K. Alsaih, S. S. A. Ali, and F. Meriaudeau, "Evaluation of deep neural networks for semantic segmentation of prostate in T2W MRI," *Sensors*, vol. 20, no. 11, p. 3183, Jun. 2020.

[174] Q. Liu, Q. Dou, and P.-A. Heng, "Shape-aware meta-learning for generalizing prostate MRI segmentation to unseen domains," 2020, *arXiv:2007.02035*. [Online]. Available: http://arxiv.org/abs/2007.02035

[175] O. Yaniv, O. Portnoy, A. Talmon, N. Kiryati, E. Konen, and A. Mayer, "V-Net light–parameter-efficient 3-D convolutional neural network for prostate MRI segmentation," in *Proc. IEEE 17th Int. Symp. Biomed. Imag. (ISBI)*, Apr. 2020, pp. 442–445.

[176] D. Singh, V. Kumar, C. J. Das, A. Singh, and A. Mehndiratta, "Segmentation of prostate zones using probabilistic atlas-based method with diffusion-weighted MR images," *Comput. Methods Programs Biomed.*, vol. 196, Nov. 2020, Art. no. 105572.

[177] Z. Lu, M. Zhao, and Y. Pang, "CDA-Net for automatic prostate segmentation in MR images," *Appl. Sci.*, vol. 10, no. 19, p. 6678, Sep. 2020.

[178] P. Hambarde, S. Talbar, A. Mahajan, S. Chavan, M. Thakur, and N. Sable, "Prostate lesion segmentation in MR images using radiomics based deeply supervised U-Net," *Biocybernetics Biomed. Eng.*, vol. 40, no. 4, pp. 1421–1435, Oct. 2020.

[179] X. Qin, Y. Zhu, W. Wang, S. Gui, B. Zheng, and P. Wang, "3D multi-scale discriminative network with multi-directional edge loss for prostate zonal segmentation in bi-parametric MR images," *Neurocomputing*, vol. 418, pp. 148–161, Dec. 2020.

[180] Q. Liu, Q. Dou, L. Yu, and P. A. Heng, "MS-Net: Multi-site network for improving prostate segmentation with heterogeneous MRI data," *IEEE Trans. Med. Imag.*, vol. 39, no. 9, pp. 2713–2724, Sep. 2020.

[181] O. Zavala-Romero, A. L. Breto, I. R. Xu, Y.-C. C. Chang, N. Gautney, A. D. Pra, M. C. Abramowitz, A. Pollack, and R. Stoyanova, "Segmentation of prostate and prostate zones using deep learning: A multi-MRI vendor analysis," *Strahlentherapie und Onkologie*, vol. 196, no. 10, pp. 932–942, 2020.

[182] Q. Zhu, B. Du, B. Turkbey, P. Choyke, and P. Yan, "Exploiting interslice correlation for MRI prostate image segmentation, from recursive neural networks aspect," *Complexity*, vol. 2018, pp. 1–10, Feb. 2018.

[183] A. M. Feldman, Z. Dai, E. Carver, C. Liu, J. K. Lee, M. Pantelic, M. A. Elshaikh, and N. Wen, "Utilizing a deep learning-based object detection and instance segmentation algorithm for the delineation of prostate and prostate cancer segmentation," *Int. J. Radiat. Oncol., Biol., Phys.*, vol. 105, no. 1, pp. S197–S198, 2019.

[184] Z. Dai, E. Carver, C. Liu, J. Lee, A. Feldman, W. Zong, M. Pantelic, M. Elshaikh, and N. Wen, "Segmentation of the prostatic gland and the intraprostatic lesions on multiparametic MRI using mask R-CNN," *Adv. Radiat. Oncol.*, vol. 5, no. 3, pp. 473–481, 2020.

[185] P. Lapa, M. Castelli, I. Gonçalves, E. Sala, and L. Rundo, "A hybrid end-to-end approach integrating conditional random fields into CNNs for prostate cancer detection on MRI," *Appl. Sci.*, vol. 10, no. 1, p. 338, Jan. 2020.

[186] I. Goodfellow, J. Pouget-Abadie, M. Mirza, B. Xu, D. Warde-Farley, S. Ozair, A. Courville, and Y. Bengio, "Generative adversarial nets," in *Proc. Adv. Neural Inf. Process. Syst.*, 2014, pp. 2672–2680.

[187] S. Kohl, D. Bonekamp, H.-P. Schlemmer, K. Yaqubi, M. Hohenfellner, B. Hadaschik, J.-P. Radtke, and K. Maier-Hein, "Adversarial networks for the detection of aggressive prostate cancer," 2017, *arXiv:1702.08014*. [Online]. Available: http://arxiv.org/abs/1702.08014

[188] H. Jia, Y. Xia, Y. Song, D. Zhang, H. Huang, Y. Zhang, and W. Cai, "3D APA-Net: 3D adversarial pyramid anisotropic convolutional network for prostate segmentation in MR images," *IEEE Trans. Med. Imag.*, vol. 39, no. 2, pp. 447–457, Feb. 2020.

[189] G. Zhang, W. Wang, D. Yang, J. Luo, P. He, Y. Wang, Y. Luo, B. Zhao, and J. Lu, "A bi-attention adversarial network for prostate cancer segmentation," *IEEE Access*, vol. 7, pp. 131448–131458, 2019.

[190] A. Grall, A. Hamidinekoo, P. Malcolm, and R. Zwiggelaar, "Using a conditional generative adversarial network (cGAN) for prostate segmentation," in *Proc. Annu. Conf. Med. Image Understand. Anal.* Cham, Switzerland: Springer, 2019, pp. 15–25.

[191] D. Nie and D. Shen, "Adversarial confidence learning for medical image segmentation and synthesis," *Int. J. Comput. Vis.*, vol. 128, pp. 1–20, Nov. 2020.

[192] K. B. Girum, G. Créhange, R. Hussain, P. M. Walker, and A. Lalande, "Deep generative model-driven multimodal prostate segmentation in radiotherapy," in *Proc. Workshop Artif. Intell. Radiat. Therapy*. Cham, Switzerland: Springer, 2019, pp. 119–127.

[193] H. Jia, Y. Song, D. Zhang, H. Huang, D. Feng, M. Fulham, Y. Xia, and W. Cai, "3D global convolutional adversarial network for prostate MR volume segmentation," 2018, *arXiv:1807.06742*. [Online]. Available: http://arxiv.org/abs/1807.06742

[194] X. Hu, A. G. Chung, P. Fieguth, F. Khalvati, M. A. Haider, and A. Wong, "ProstateGAN: Mitigating data bias via prostate diffusion imaging synthesis with generative adversarial networks," 2018, *arXiv:1811.05817*. [Online]. Available: http://arxiv.org/abs/1811.05817
[195] U. C. Birbiri, A. Hamidinekoo, A. Grall, P. Malcolm, and R. Zwiggelaar, "Investigating the performance of generative adversarial networks for prostate tissue detection and segmentation," *J. Imag.*, vol. 6, no. 9, p. 83, Aug. 2020.
[196] W. Wang, G. Wang, X. Wu, X. Ding, X. Cao, L. Wang, J. Zhang, and P. Wang, "Automatic segmentation of prostate magnetic resonance imaging using generative adversarial networks," *Clin. Imag.*, vol. 70, pp. 1–9, Feb. 2021.
[197] F. Bray, J. Ferlay, I. Soerjomataram, R. L. Siegel, L. A. Torre, and A. Jemal, "Global cancer statistics 2018: GLOBOCAN estimates of incidence and mortality worldwide for 36 cancers in 185 countries," *CA, Cancer J. Clinicians*, vol. 68, no. 6, pp. 394–424, Nov. 2018.
[198] A. E.-S. Bosaily, C. Parker, L. C. Brown, R. Gabe, R. G. Hindley, R. Kaplan, M. Emberton, and H. U. Ahmed, "PROMIS—Prostate MR imaging study: A paired validating cohort study evaluating the role of multi-parametric MRI in men with clinical suspicion of prostate cancer," *Contemp. Clin. Trials*, vol. 42, pp. 26–40, May 2015.
[199] S. Verma, B. Turkbey, N. Muradyan, A. Rajesh, F. Cornud, M. A. Haider, P. L. Choyke, and M. Harisinghani, "Overview of dynamic contrast-enhanced MRI in prostate cancer diagnosis and management," *Amer. J. Roentgenol.*, vol. 198, no. 6, pp. 1277–1288, Jun. 2012.
[200] B. Zelhof, M. Lowry, G. Rodrigues, S. Kraus, and L. Turnbull, "Description of magnetic resonance imaging-derived enhancement variables in pathologically confirmed prostate cancer and normal peripheral zone regions," *BJU Int.*, vol. 104, no. 5, pp. 621–627, Sep. 2009.
[201] N. A. Parra, A. Pollack, F. M. Chinea, M. C. Abramowitz, B. Marples, F. Munera, R. Castillo, O. N. Kryvenko, S. Punnen, and R. Stoyanova, "Automatic detection and quantitative DCE-MRI scoring of prostate cancer aggressiveness," *Frontiers Oncol.*, vol. 7, p. 259, Nov. 2017.
[202] S. G. Armato, "PROSTATEx Challenges for computerized classification of prostate lesions from multiparametric magnetic resonance images," *J. Med. Imag.*, vol. 5, no. 4, 2018, Art. no. 044501.
[203] M. D. Greer, N. Lay, J. H. Shih, T. Barrett, L. K. Bittencourt, S. Borofsky, I. Kabakus, Y. M. Law, J. Marko, H. Shebel, F. V. Mertan, M. J. Merino, B. J. Wood, P. A. Pinto, R. M. Summers, P. L. Choyke, and B. Turkbey, "Computer-aided diagnosis prior to conventional interpretation of prostate mpMRI: An international multi-reader study," *Eur. Radiol.*, vol. 28, no. 10, pp. 4407–4417, Oct. 2018.
[204] H. U. Ahmed, A. E.-S. Bosaily, L. C. Brown, R. Gabe, R. Kaplan, M. K. Parmar, Y. Collaco-Moraes, K. Ward, R. G. Hindley, A. Freeman, A. P. Kirkham, R. Oldroyd, C. Parker, and M. Emberton, "Diagnostic accuracy of multi-parametric MRI and TRUS biopsy in prostate cancer (PROMIS): A paired validating confirmatory study," *Lancet*, vol. 389, no. 10071, pp. 815–822, Feb. 2017.
[205] V. Kasivisvanathan, "MRI-targeted or standard biopsy for prostate-cancer diagnosis," *New England J. Med.*, vol. 378, no. 19, pp. 1767–1777, 2018.
[206] G. Litjens *et al.*, "Evaluation of prostate segmentation algorithms for MRI: The PROMISE12 challenge," *Med. Image Anal.*, vol. 18, no. 2, pp. 359–373, Feb. 2014.
[207] Y. LeCun, Y. Bengio, and G. Hinton, "Deep learning," *Nature*, vol. 521, no. 7553, pp. 436–444, May 2015.
[208] P. Isola, J.-Y. Zhu, T. Zhou, and A. A. Efros, "Image-to-image translation with conditional adversarial networks," in *Proc. IEEE Conf. Comput. Vis. Pattern Recognit.*, Jul. 2017, pp. 1125–1134.
[209] J. Ma, "Segmentation loss odyssey," 2020, *arXiv:2005.13449*. [Online]. Available: http://arxiv.org/abs/2005.13449
[210] T.-Y. Lin, P. Goyal, R. Girshick, K. He, and P. Dollar, "Focal loss for dense object detection," in *Proc. IEEE Int. Conf. Comput. Vis. (ICCV)*, Oct. 2017, pp. 2980–2988.
[211] Z. Zheng, P. Wang, W. Liu, J. Li, R. Ye, and D. Ren, "Distance-IoU loss: Faster and better learning for bounding box regression," 2019, *arXiv:1911.08287*. [Online]. Available: http://arxiv.org/abs/1911.08287
[212] H. Kervadec, J. Bouchtiba, C. Desrosiers, E. Granger, J. Dolz, and I. B. Ayed, "Boundary loss for highly unbalanced segmentation," in *Proc. Int. Conf. Med. Imag. Deep Learn.*, 2019, pp. 285–296.
[213] Y. Boykov, V. Kolmogorov, D. Cremers, and A. Delong, "An integral solution to surface evolution PDEs via geo-cuts," in *Proc. Eur. Conf. Comput. Vis.* Berlin, Germany: Springer, 2006, pp. 409–422.
[214] W. Zhu, Y. Huang, L. Zeng, X. Chen, Y. Liu, Z. Qian, N. Du, W. Fan, and X. Xie, "AnatomyNet: Deep learning for fast and fully automated whole-volume segmentation of head and neck anatomy," *Med. Phys.*, vol. 46, no. 2, pp. 576–589, Feb. 2019.
[215] C. N. dos Santos, I. Padhi, P. Dognin, and Y. Mroueh, "Generative feature matching networks," in *Proc. Int. Conf. Learn. Represent. (ICLR)*, New Orleans, LA, USA, May 2019, pp. 1–22. [Online]. Available: https://iclr.cc/Conferences/2019
[216] V. Yeghiazaryan and I. D. Voiculescu, "Family of boundary overlap metrics for the evaluation of medical image segmentation," *J. Med. Imag.*, vol. 5, no. 1, 2018, Art. no. 015006.
[217] A. A. Taha and A. Hanbury, "Metrics for evaluating 3D medical image segmentation: Analysis, selection, and tool," *BMC Med. Imag.*, vol. 15, no. 1, p. 29, Dec. 2015.
[218] M. G. Linguraru, J. A. Pura, V. Pamulapati, and R. M. Summers, "Statistical 4D graphs for multi-organ abdominal segmentation from multiphase CT," *Med. Image Anal.*, vol. 16, no. 4, pp. 904–914, May 2012.
[219] G. Litjens, O. Debats, J. Barentsz, N. Karssemeijer, and H. Huisman, "Computer-aided detection of prostate cancer in MRI," *IEEE Trans. Med. Imag.*, vol. 33, no. 5, pp. 1083–1092, May 2014.

ZIA KHAN received the bachelor's degree in electrical and electronics engineering from Sarhad University, Peshawar, Pakistan, in 2013, and the master's degree in electrical and electronics engineering from the Universiti Teknologi PETRONAS (UTP), Malaysia, in 2020. His research interests include application machine learning, deep learning, and prostate MRI segmentation.

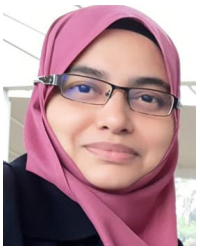

NORASHIKIN YAHYA (Member, IEEE) received the B.Eng. degree (Hons.) in electronic engineering from The University of Sheffield, U.K., in 2001, the M.Sc. degree in electrical engineering from Lehigh University, USA, in 2004, and the Ph.D. degree in electrical engineering from Universiti Teknologi PETRONAS (UTP), Malaysia, in 2015. She is currently a Senior Lecturer with UTP and also a member of the Centre for Intelligent Signal and Imaging Research (CISIR) Laboratory, one of the Malaysia National Higher Institution Centre of Excellence (HICoE) status focusing on neuro signal and image analysis as its research niche area. Her current research interests include image segmentation and pattern recognition techniques involving biomedical signals and images, seismic signals, and acoustic emission signals using deep learning architecture.

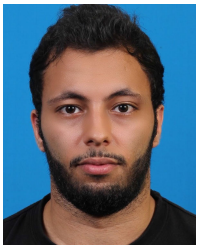

KHALED ALSAIH received the bachelor's degree in electronics engineering majoring in biomedical-instrumentation engineering from Multimedia University, Malaysia, in 2014, the dual master's degree in computer vision, robotics, and mechatronics from the University of Technology Malaysia and Universite Bourgogne Franche-Comté, France, in 2016, and the Ph.D. degree in electrical and electronics engineering from Universiti Teknologi PETRONAS (UTP), Malaysia, in 2020. He is currently holding a postdoctoral position with the Universite de Lyon in Laboratoire Hubert Curien, Saint-Etienne, France. His research interests include artificial intelligence, retinal disease segmentation and classification, image and signal processing, medical imaging, and deep learning.

MOHAMMED ISAM AL-HIYALI received the B.Eng. degree in laser and optoelectronics engineering from Al-Nahrain University, Iraq, in 2010, and the master's degree in biomedical engineering from Universiti Putra Malaysia (UPM), Malaysia, in 2019. He is currently pursuing the Ph.D. degree with Universiti Teknologi PETRONAS (UTP), Malaysia. His research interests include artificial intelligence, image and signal processing, medical imaging, and deep learning.

FABRICE MERIAUDEAU (Member, IEEE) was born in March 1971. He received the master's degree in physics from Dijon University, France, the Engineering degree (Hons.) in material sciences, in 1994, and the Ph.D. degree in image processing from Dijon University, in 1997. He held a postdoctoral position for a year at The Oak Ridge National Laboratory. He coordinated an Erasmus Mundus Master in the field of computer vision and robotics, from 2006 to 2010. He was the Vice President for International Affairs with the University of Burgundy, from 2010 to 2012. From 2011 to 2016, he was the Director of the Le2i (UMR CNRS), France, which had more than 200 staff members. From 2017 to 2018, he was the Director of the Institute Health and Analytics, Universiti Teknologi PETRONAS Malaysia. He is currently a Professeur des Universites with the University of Burgundy, ImVia Research Group, where he leads the Artificial Intelligence theme. He has authored or coauthored more than 150 international publications and holds three patents. His research interests include image processing for non-conventional imaging systems (UV, IR, and polarization) and more recently on medical/biomedical imaging.